Biochemical and structural insights into the auto-inhibited state of Mical1 and its activation by Rab8

Amrita Rai[1,*], Petra Janning[2], Ingrid R. Vetter[3] and Roger S. Goody[1]

[1]Department of Structural Biochemistry, Max Planck Institute of Molecular Physiology, Otto-Hahn-Strasse 11, 44227 Dortmund, Germany

[2]Department of Chemical Biology, Max Planck Institute of Molecular Physiology, Otto-Hahn-Strasse 11, 44227 Dortmund, Germany

[3]Department of Mechanistic Cell Biology, Max Planck Institute of Molecular Physiology, Otto-Hahn-Strasse 11, 44227 Dortmund, Germany

[*]Corresponding author: Amrita Rai (amrita.rai@mpi-dortmund.mpg.de)

Abstract

Mical1 regulates F-actin dynamics through the reversible oxidation of actin, a process controlled by its interactions with various proteins. Upon binding to Rab8 family members, Mical1 links endosomes to the cytoskeleton, promoting F-actin disassembly. In the absence of Rab, Mical1 exists in an auto-inhibited state, but its biochemical characterization remains incomplete. Our study reveals that the N-terminal MO-CH-LIM domains of Mical1 form an intramolecular complex with its C-terminal bMERB domain. Mutational analysis, guided by the AlphaFold2 model, identifies critical residues at the binding interface. Additionally, we demonstrate that full-length Mical1 binds to Rab8 in a 1:2 stoichiometry, thereby releasing auto-inhibition. Through structure-based mutational studies, we uncover allostery between the N and C-terminal Rab binding sites. Notably, Rab binding at the high-affinity C-terminal site precedes binding at the N-terminal site, suggesting a sequential binding mode. These findings elucidate how Rab8 binding releases the MO-CH-LIM domains from the Mical1 bMERB domain, facilitating interactions with other proteins and the actin cytoskeleton, thereby modulating actin dynamics.

Keywords: Mical1; Rab8, Rab10; Rab effectors; auto-inhibition; F-actin; human; biochemistry; biophysics; structural biology

Introduction

Actin dynamics is a highly controlled process, and the precise assembly and disassembly of actin is necessary for many cellular processes, including motility, adhesion, morphogenesis, and cytokinesis[1-3]. Actin-binding proteins (ABPs) are known to control filament polymerization (F-actin), its organization (bundling), and actin disassembly (G-actin). Apart from ABPs, actin post-translational modifications such as phosphorylation, oxidation, acetylation, arginylation, SUMOylation, ubiquitination, and others, regulate actin dynamics, fine-tune actin organization, and its interaction with ABPs[4]. The Molecule Interacting with CasL (Mical) protein family members include Mical1, Mical2, and Mical3, which are monooxygenases that oxidize actin and regulate cytoskeleton organization in the presence of the coenzyme NADPH and of O_2[5]. Mical1 specifically oxidizes Met44 and Met47 of the DNaseI-binding loop (D-loop) in actin monomers[6]. These residues are involved in bridging actin subunits, thereby regulating F-actin stability[6]. Methionine oxidation leads to F-actin depolymerization, a process that can be selectively reversed by methionine sulfoxide reductases. For example, MsrB reduces Met44 and Met47 of oxidized monomeric actin (G-actin), leading to the repolymerization of actin[7,8]. Mical proteins play a crucial role in actin assembly regulation during muscle organization, axon guidance, drosophila bristle development, cell shape, cell viability, cardiovascular integrity, vesicular trafficking, and regulation of nuclear actin[9]. Mical1 has been implicated in several different cancers, including pancreatic[10], breast[11], gastric[12], colorectal[13], and melanoma[14] as well as in neurological and mental health disorders such as neurodegeneration[15], spinal cord injury[16], and epilepsy[17].

Mical family members contain an N-terminal monooxygenase (MO) domain which plays a crucial role in actin-depolymerization, a calponin homology (CH) domain, a LIM (Lin-11, Isl-1, and Mec-3) domain which provides a protein-protein interaction interface, and a C-terminal bMERB domain that interacts with Rab proteins[5,18]. Apart from these domains, Mical family members have a proline-rich region that interacts with SH3 domain-containing proteins[19]. Mical1 plays a crucial role in synapse development[20]. Mical1 and Mical3 are required for cytokinesis and vesicular trafficking. They regulate these processes by regulating F-actin dynamics by disassembling the actin filaments. Mical-like (MICAL-L) family members lack the MO domain and play critical roles in vesicular trafficking[21]. Humans have two Mical-like proteins (Mical-L1 and Mical-L2/JRAB) whereas Drosophila has a single Mical and a single Mical-like protein. Several studies have reported that in the absence of stimuli, the Micals and Mical-like family members exist in an auto-inhibited state[9]. However, biochemical, and structural characterization of the auto-inhibited state is missing.

Rab GTPases are players that have a crucial role in vesicular trafficking and more than 60 Rabs have been reported for humans[22]. Similar to other small GTPases, they act as molecular switches, switching

between GTP-bound active state and GDP-bound inactive state[22]. The switching process is spatiotemporally regulated by guanine nucleotide exchange factors (GEFs) which facilitate the nucleotide exchange from GDP to GTP and their GTPase activity is enhanced by GTPase-activating proteins (GAPs)[23-25]. In the active GTP bound state, Rabs interacts with specific effector molecules to execute distinct downstream functions[22]. MICAL family members are one such Rab8 family effector. It has been shown that the binding of Rab molecules activates these family members by releasing auto-inhibition[26,27]. We have previously shown that in the case of some family members, such as Mical1/3 and EHBP1L1, Rab binds to the bMERB domain in a 1:2 stoichiometry, whereas other bMERB family members have only a C-terminal high affinity binding site[28-30]. However, it is still to be shown whether full-length Mical1 binds to two Rab molecules and if there is any allosteric interaction between the two binding sites.

In this study, we comprehensively characterized the auto-inhibited and active states of human Mical1 using biochemical and structural methods. Via isothermal titration calorimetry (ITC), we confirmed that the N-terminal MO-CH-LIM domains interact with the C-terminal bMERB domain, requiring the full-length bMERB domain for this interaction. Crosslinking-mass spectrometry (XL-MS) experiments supported the auto-inhibited state of Mical1. Utilizing AlphaFold2[31], we constructed a model revealing the auto-inhibited state and identified crucial interacting residues. Additionally, we confirmed the 1:2 stoichiometry of Rab8a binding to full-length Mical1. Next, we investigated whether allostery exists in the N- and C-terminal Rab binding sites. To answer this, we have used the bMERB domain, since it shows similar Rab affinity as full-length Mical1. Biochemical experiments show that Rab8 first binds to the high-affinity C-terminal site, facilitating subsequent second Rab8 binding to the low-affinity N-terminal site. These findings underscore the essential role of Rab binding in Mical1 activation.

Results and Discussion

Mical1 exists in an auto-inhibited state

Human Mical1 contains four domains: an N-terminal monooxygenase (MO) domain, a central calponin (CH), and a Lin-11, Islet-1, and Mec-3 (LIM) domain, and a C-terminal bivalent Mical/EHBP Rab-binding (bMERB) domain. The UniProt database documents four Mical1 isoforms, and for our work, the domain boundaries are taken from isoform 1 (Q8TDZ2) (Supplementary Fig. 1). To characterize the auto-inhibited and active states, we purified full-length as well as different deletion constructs of Mical1 isoform1 (Fig. 1a and Supplementary Table. 2). Full-length Mical1, MO-CH-LIM, MO-CH, and the MO domain have a C-terminal histidine tag, while the bMERB domain is tag-free. Further, to determine the oligomeric states of the proteins, their native masses were determined by size

exclusion chromatography combined with multi-angle light scattering analysis (SEC-MALS). It was found that all the purified constructs predominantly exist as monomers. The purified full-length Mical1, MO-CH-LIM (residues 1-781), MO-CH (residues 1-615); MO (residues 1-488), and bMERB (residues 918-1067) domain showed average molar masses of 112.2 kDa (theoretical mass: 118.94 kDa), 86.2 kDa (theoretical mass: 86.48 kDa), 69.4 kDa (theoretical mass: 68.23 kDa), 55.78 kDa (theoretical mass: 55.14 kDa), 18.13 kDa (theoretical mass: 17.83 kDa), respectively (Fig. 1b-f).

Several studies have indicated that, in the absence of Rab, the bMERB domain forms an intramolecular interaction with the other domains (CH/LIM/MO-CH-LIM)[26,32-35]. Mical-like family members form intramolecular auto-inhibited complexes between their N-terminal CH domain (Mical-L1)[32] or LIM domain (Mical-L2)[34] and their C-terminal bMERB domain. It has been observed that full-length Mical is catalytically inactive, with its enzyme activity somehow inhibited by the C-terminal domain[36]. Fremont *et al*., proposed their Mical1 auto-inhibited model based on their F-actin depolymerization assay and cell biology data. This model suggests that the N-terminal monooxygenase, along with the CH and LIM domains (MO-CH-LIM), interacts with the bMERB domain, forming an enzymatically inactive complex[26]. The binding of Rab releases auto-inhibition, resulting in F-actin depolymerization[26,36,37]. However, the biochemistry of the Mical1 auto-inhibited state is not well understood. Therefore, we set out to systematically confirm and quantify the intramolecular interaction between the N and C-terminal domains of Mical1. To address this, we first investigated the interaction between the separately purified C-terminal bMERB domain and the N-terminal MO/MO-CH/MO-CH-LIM domains via ITC. We observed binding between the MO-CH-LIM domain construct and the bMERB domain. The binding is enthalpy-driven, characterized by a K_D value of 2.7 ± 0.16 µM and a 1:1 stoichiometry. However, no binding was observed between the isolated bMERB domain and the MO-CH/MO domains (Fig. 1g-i). Previously, we demonstrated that the Mical1 CH-LIM construct and the isolated CH and LIM domains do not interact with the Mical1 bMERB domain[30]. Therefore, our data suggest that all three domains (MO-CH-LIM) are required for bMERB interaction (Fig. 1g-i), forming a stable complex. Apart from bMERB family members, other F-actin interacting proteins exist in an auto-inhibited state. Examples are, MyosinV, Talin2, and Vinculin, and their activation is spatially and temporally regulated[38,39].

Full-length bMERB domain is essential for MO-CH-LIM interaction

Earlier, we reported that some bMERB family members, such as the Mical1 and Mical3 bMERB domains, have two Rab-binding sites: a high-affinity C-terminal binding site (Ct-RBS2; helices 2-3) and a lower or similar-affinity N-terminal binding site (Nt-RBS1; helices 1-2). In contrast, the EHBP1L1 bMERB domain has two Rab-binding sites with similar affinities[28,29]. Another bMERB family member, EHBP1, which has a single Rab-binding site, forms an auto-inhibited bMERB complex. In this complex,

helices 1-2 of the bMERB domain constitute the CH binding site, and the binding of Rab at the C-terminal binding site (helices 2-3) releases the auto-inhibition[30].

To pinpoint the exact binding site on Mical1, we generated two deletion constructs of the Mical1 bMERB domain in which either the N or the C-terminal helix was deleted and checked its interaction with the MO-CH-LIM. Our ITC data clearly show that the full-length bMERB domain is essential for the interaction, and the N- and C-terminal deletion constructs fail to form a stable complex (Fig. 2a-c).

To independently verify the interaction between the MO-CH-LIM and the bMERB domains, we performed crosslinking mass spectrometry (XL-MS) analyses. We conducted two experiments: for the first experiment, full-length Mical1 was used, and for the second experiment, the MO-CH-LIM (residues 1-781) and the bMERB (residues 918-1067) domain were mixed in a 1:2 ratio to obtain saturated MO-CH-LIM:bMERB complex (Fig. 2d-f). A total of 59 peptides were identified from Mical1 full-length experiments, and 76 peptides were identified from the MO-CH-LIM:bMERB complex. Crosslinks were mapped, revealing numerous inter-domain and intra-domain cross-links. Cross-links between the two experiments were highly reproducible. However, only 6 peptides between the MO and bMERB domains were observed in the Mical1 full-length experiment, whereas 24 peptides between the MO and bMERB domains were observed in the MO-CH-LIM:bMERB complex experiment. Cross-linking peptides show that the full-length bMERB domain interacts with the MO domain, which is in good agreement with our ITC data, suggesting that all three helices of the bMERB domain were involved in the interaction. However, we did not observe any cross-links between the CH and bMERB domains, or the LIM and bMERB domains. Our ITC data clearly showed that the MO-CH-LIM construct interacts with the bMERB domain but not MO or MO-CH. The absence of cross-links could be attributed to the lower number of lysine residues in the CH and LIM domains; only two lysine residues are present in the CH domain, and one is present in the LIM domain. Perhaps they are not part of the binding interface, or the low number of lysine residues results in no cross-links. However, XL-MS experiments show that the bMERB domain interacts with the MO domain, suggesting the formation of an intramolecular complex.

Structural basis of Mical1 auto-inhibition

To understand the molecular basis of how the MO-CH-LIM domains bind to the bMERB domain, we attempted to crystallize both full-length Mical1 and the MO-CH-LIM:bMERB complex. Crystals were obtained for the MO-CH-LIM:bMERB complex; however, they did not diffract well. Despite several attempts, we were unable to crystalize full-length Mical1. Subsequently, we utilized AlphaFold2[31] modeling to predict the auto-inhibited state of Mical1. The resulting model, characterized by high

confidence predicted local difference distance test (pLDDT) scores and predicted alignment errors (PAE), was analyzed in detail (Fig. 3a and Supplementary Fig. 2)

The AlphaFold2 model clearly predicts that the MO (residues 1-488), CH (residues 508-613), a helix connecting the CH and LIM domain ($Helix^{CHL}$; residues 624-654), LIM (residues 692-751) domains and linker (residues 800-855) interact with the C-terminal bMERB domain, forming an auto-inhibited complex. Helices 1-2 of the bMERB (residues 886-1067) domain are involved in interactions with the MO, CH, and LIM domains, whereas helix 3 interacts specifically with $Helix^{CHL}$, resulting in three distinct binding interfaces on the bMERB domain. The binding interfaces predominantly consist of hydrophobic interactions (Fig. 3a-c). The first binding interface involves the first half of helix 1 and the second half of helix 2 of the bMERB domain, where the MO domain interacts (1190 $Å^2$ buried surface between MO and bMERB domain). The MO domain consists of two core domains: a large domain (MO^{Large_domain}, residues 1–226 and 374–484) and a smaller cap domain (MO^{Cap_domain}, residues 235–366). Both domains are connected by β-strands β9 (residues 228–234) and β15 (residues 367–373). The active site is a cleft formed by both the MO^{Large_domain} and the MO^{Cap_domain}, containing a FAD molecule. Both the MO^{Large_domain} and the MO^{Cap_domain} interact with the bMERB domain. The MO^{Large_domain} interacts with helix 1, whereas the MO^{Cap_domain} interacts with both helices 1 and 2 (Fig. 3d,e). The binding site is opposite to the active site (FAD binding cleft). The second binding interface lies in the center of the bMERB domain and involves all three helices of the bMERB domain. At this interface, the MO^{Cap_domain}, LIM domain, and the $Helix^{CHL}$ interact. The third binding interface involves helices 1-2 of bMERB. At this interface, the CH (507 $Å^2$) and LIM (652 $Å^2$) domains interact (Fig. 3f). Although helix 3 of the bMERB domain does not directly interact with the MO, CH, and LIM domains, our ITC data clearly show that helix 3 is required for complex formation. This could be attributed to the interaction between helices 2 and 3 of the bMERB domain and the $Helix^{CHL}$, suggesting that this interaction stabilizes the second binding interface, where the MO and LIM domains interact with helices 1 and 2 of the bMERB domain (Fig. 3a).

Apart from the active site binding cleft, another smaller cleft is formed by the MO^{Large_domain} and the MO^{Cap_domain}, and helix 1 of the bMERB domain occupies this cleft (Fig. 3d). This cleft is formed by the loops connecting β9-β10, β17-α15, and β15 of the MO^{Large_domain}, and β11 and the loop connecting α10-11 of the MO^{Cap_domain}. K918 of helix 1 forms hydrogen bond interactions with D153 and E257 of the MO domain. E921 forms a hydrogen bond interaction with S259 of the MO domain (Fig. 3a, inset1). The side chain of F925 of the bMERB domain inserts itself into the hydrophobic patch formed by P401, L402, and V285 residues of the MO domain. On the other side, the side chain of I264 of the MO^{Cap_domain} inserts itself into the hydrophobic patch created by helix 1 (I931) and helix 2 (V995 and L998), and

Y265 of the MO^{Cap_domain} forms a hydrophobic interaction with F925 (Fig. 3a, inset1). The K235 residue of the loop connecting β9-β10 forms a hydrogen bond with E939 (Fig. 3a, inset4).

Both the CH and LIM domain binding sites are formed by the C-terminal half of helix 1 and the N-terminal half of helix 2 of the bMERB domain. This binding interface is characterized by a contiguous array of hydrophobic residues. $L598^{CH}$ engages in hydrophobic interactions with L956, V971, and L974 of the bMERB domain, whereas $I601^{CH}$ interacts hydrophobically with L975 and V978 of the bMERB domain. Additionally, the CH:bMERB interaction is reinforced by hydrogen bonds between residues $D596^{CH}$-R957 and $E512^{CH}$-K988 (Fig. 3a, inset2). V632 and F634 of $Helix^{CHL}$ form hydrophobic interactions with V985, I993, L1047, and F1050 of bMERB domain (Fig. 3a, inset5). Extensive hydrophobic interactions occur between the LIM domain and the bMERB domain. $Y705^{LIM}$ forms hydrophobic interactions with V950 and L954, while the side chain of $L707^{LIM}$ inserts itself into the hydrophobic groove created by L974, L977, and V978. Similarly, $W732^{LIM}$ engages in hydrophobic interactions with L935 and M992. Furthermore, several hydrogen bond interactions are observed between residues $R719^{LIM}$-E988 and $T730^{LIM}$-E939 (Fig. 3a, inset3-4).

Next, we compared the auto-inhibited Mical1 model with previously published crystal structures of Mical1 individual domains[26,40-42]. The predicted MO domain is nearly identical to the isolated mouse Mical1 MO domain (oxidized state; PDB: 2BRY), with an RMSD of 0.299 Å for 396 Cα residues and an RMSD of 0.581 Å for 422 Cα residues in the NADPH-reduced mouse Mical1 MO domain(reduced state; PDB: 2C4C)[40] (Supplementary Fig. 3a-b). Although the AlphaFold-generated model clearly lacks FAD, the conformation of the active site residues is similar to that of the mouse Mical1 MO domain (oxidized state) (Fig. 3e). However, even in the auto-inhibited state model, the active site remains accessible for the catalytic reaction. Previously, it has been shown that in the reduced state of the MO domain, the isoalloxazine ring of the FAD flips during the catalytic cycle, leading to conformational changes in active site residues[40]. Conformational changes were observed upon NADPH binding for the residues F399, W400, and P401 (Fig. 3d-e). F399 undergoes major changes as it flips upon NADPH treatment. In the auto-inhibited AlphaFold2 model, this rotation is sterically hindered by bMERB domain binding, suggesting that MO:bMERB domain binding stabilizes the oxidized state of the MO domain, and steric hindrance prevents FAD conversion from oxidized to reduced state (Fig. 3d-e). The side chains of I264 and Y265 of the MO^{Cap_domain} in the auto-inhibited state, are inserted into a hydrophobic patch created by helices 1 and 2 of the bMERB domain. In the isolated oxidized/reduced mouse MO domain structure, the Y265 side chain lacked electron density, and there was no electron density observed for I264. This suggests that binding with bMERB could stabilize the loop conformation of the MO domain (Fig. 3d-e).

Furthermore, structural analysis of isolated human CH (PDB: 2DK9) and bMERB domain (PDB: 5LE0) revealed differences to the AlphaFold2 predicted CH and bMERB domains, with an rmsd of 1.089 for 92 Cα residues for the CH domain and an rmsd of 0.967 Å for 94 Cα residues for the bMERB domain[26,41]. Notably, the maximum structural difference was observed for the isolated human LIM domain (PDB: 2CO8), with an rmsd of 2.135 Å for 65 Cα residues[42] (Supplementary Fig. 3c-f). We hypothesize that the initial interaction occurs between the bMERB domain and the CH domain, establishing the binding interface for subsequent engagement with the LIM domain. As the LIM domain binds to this interface, it brings all three domains into close proximity. These bMERB:CH interactions stabilize the MO binding interface, creating a compact structure. Finally, the MO domain interacts with both the bMERB and LIM domains, facilitating the formation of a tightly packed auto-inhibited complex.

Generation of bMERB interface mutants

To corroborate the prediction of the Mical1 auto-inhibited AlphaFold2 model, we conducted biochemical experiments. The sequence alignment of bMERB domains shows that the surface residues interacting with MO-CH-LIM are highly conserved among different mammalian homologs (Supplementary Fig. 4). To grasp the significance of individual interface residues, we introduced mutations guided by the AlphaFold2 Mical1 auto-inhibited model into each helix of the bMERB domain and monitored their interaction with the MO-CH-LIM via ITC experiments (Fig. 4). All bMERB mutants with mutations of conserved residues to alanine, except for the K918A_E921A double mutant, show a significant decrease in binding affinity. Double alanine mutations in helix 1 of the bMERB domain (K918A and E921A) result in only a 2-fold reduction in binding affinity with the MO-CH-LIM (Fig. 4c). K918 forms a hydrogen bond with D153 and E257 of the MO domain, whereas E921 forms a hydrogen bond with the S259 of the MO domain. In contrast, mutation of F925 abrogates the MO-CH-LIM interaction (Fig. 4d). The F925 side-chain inserts itself into the hydrophobic pocket created by A262, Y265, and V285 of the MO domain. The E939A mutant shows more than a 5-fold reduction in binding affinity with the MO-CH-LIM. In the control experiment (E939A to buffer), there was a very high heat exchange upon dilution in the buffer, resulting in a small signal when E939A was injected into MO-CH-LIM. (Fig. 4e). The side chain of E939 forms hydrogen bonds with K235 of the MO domain and the side chain of T730 in the LIM domain.

Both double alanine mutations of helix 2 mutants (L974A_L975A and L977A_V978A) resulted in more than a 6-fold reduction in binding affinity (Fig. 4f, g). Residues L956, V971, L974, L975, L977, and V978 of the bMERB domain collectively form a hydrophobic patch that accommodates the CH and LIM domains. The side chain of L598 of the CH domain inserts itself into the hydrophobic pocket created by L956, V971, and L974 of the bMERB domain. Additionally, the side chain I601 of the CH domain establishes a hydrophobic interaction with V971 and L975. The side chain of L707 of the LIM domain

forms a hydrophobic interaction with L974, L977, and V978 of the bMERB domain. Another double alanine mutant in helix 2, M992A_I993A, led to more than a 25-fold reduction in binding affinity (Fig. 4h). M992 interacts with the LIM domain (W732), while I993 interacts with the F634 of Helix^{CHL} (624-654 aa).

Subsequently, we mutated the residues L1047 and F1050 of helix 3 to alanine, resulting in no detectable binding with the MO-CH-LIM (Fig. 4i). It is noteworthy that L1047 and F1050 do not participate in binding with the MO, CH, and LIM domains but rather with the Helix^{CHL} (residues 624-654). The side chain of F634 from the Helix^{CHL} (residues 624-654) inserts itself into the hydrophobic patch created by residues from helix 2 (I993) and helix 3 of the bMERB domain (L1047 and F1050). Additionally, the side chain of V632 from the Helix^{CHL} forms a hydrophobic interaction with V985 of the bMERB domain. The double alanine mutation of L1047 and F1050 destabilizes the hydrophobic patch of the bMERB domain.

Allostery between the two Rab binding site

We have previously demonstrated that the Mical1 bMERB domain binds to the Rab8 family member in a 1:2 stoichiometry, and the low-affinity N-terminal Rab binding site is constituted by helices 1-2 (Nt-RBS1), whereas helices 2-3 form the high-affinity Rab binding site (Ct-RBS2)[28]. Deleting either the N- or C-terminal helix demonstrated that these constructs can still bind to Rab molecules in a 1:1 stoichiometry[28]. In this study, we investigated whether two Rab molecules bind to the bMERB domain of full-length Mical1. Similar to the isolated bMERB domain, full-length Mical1 binds to Rab8 with a 1:2 stoichiometry, and the affinity is slightly lower compared to the isolated bMERB domain (K_{D1}: 40 vs 10 nM and K_{D2}: 0.73 vs 1.12 µM) (Fig. 5a-b). Next, we investigated whether the binding of Rab at either the N- or C-terminal binding site affects the other Rab binding site in the full-length bMERB domain, or if these two sites are independent. Since full-length Mical1 exhibits a similar range of Rab8 binding affinities as the isolated bMERB domain (Fig. 5b, h), we generated and purified isolated bMERB domain mutants based on the bMERB:Rab10 complex (PDB: 5LPN)[28] structure (Fig. 5c). We assessed their interaction with Rab8 by varying the bMERB:Rab ratio (1:1.1 and 1:2.2) using analytical size exclusion chromatography. These experiments aimed to identify constructs that either show no or defective complex formation or fail to display an increase in complex formation upon increasing the Rab concentration. Furthermore, the stoichiometry of the complex was determined using isothermal titration calorimetry (ITC) with selective constructs.

First, we generated mutants targeting the Nt-RBS1. Mutants K918A_E921A and F925A, as well as W970A and L974A_L975A, showed no defects (Supplementary Fig. 5a-d, h). However, mutants E939A and L956S exhibited only a slight increase in complex formation on aSEC when the bMERB:Rab ratio

was increased from 1:1.1 to 1:2.2, suggesting a lower affinity of the second N-terminal Rab binding (Supplementary Fig. 5e,f). No significant change in complex formation was observed for the mutants L977A_V978A, V978A_V985A, V978A, V985A, M992A_I993A, and L1047A_F1050A upon increasing the Rab concentration, indicating either 1:1 binding or a defect in the binding affinity of both sites (Supplementary Fig. 5i-n).

We next generated mutants targeting the Ct-RBS2. Mutants L1011S and V1038A exhibited no apparent defects. (Supplementary Fig. 6a-d). However, mutants V1041A, R1044A, and I1048A formed a smaller complex on aSEC, with no significant change observed in complex formation upon varying the Rab concentration, suggesting binding defects (Supplementary Fig. 6e-g). Notably, the double mutant V1041A_I1048A showed a major change compared to the wild type, with very little complex formation observed, indicating that these mutations affect binding at both Rab binding sites (Supplementary Fig. 6h).

Previously, distinct heat exchange patterns were observed for Rab binding at both the N-terminal and C-terminal sites of the Mical1: binding energy at the C-terminal Rab binding site is enthalpy-driven, while at the N-terminal site, Rab binding is entropy-driven[28]. To precisely determine the impact of specific mutations on Rab binding, we conducted ITC experiments with mutants: $bMERB_{V978A_V985A}$, $bMERB_{V1041A_I1048A}$, $bMERB_{M992A_I993A}$, and $bMERB_{L1047A_F1050A}$. The ITC data unequivocally demonstrate that $bMERB_{V978A_V985A}$ binds to Rab8 with a 1:1 stoichiometry, with an enthalpy-driven reaction and an affinity identical to that of Rab binding at Ct-RBS2. In contrast, binding of Rab8 to $bMERB_{V1041A_I1048A}$ results in low heat exchange, which cannot be reliably fitted, indicating that binding at the C-terminal site is a prerequisite for the second Rab binding at Nt-RBS1 (Fig. 5h-l). Residues V978/V985 and V1041/I1048 are functionally equivalent, forming hydrophobic interactions with specific residues of Rab10, including I44, W63, and F46 for V978/V1041, and L9, F46A, and I48 for V985/I1048 (Fig. 5c, Inset 1-2). Crucially, V978 and V985 are essential for N-terminal Rab binding, as evidenced by similar complex formation observed in single mutants V978A and V985A compared to the double mutant V978A_V985A. Conversely, the double mutant V1041A_I1048A exhibits a pronounced effect on Rab10 binding compared to individual mutants V1041A and I1048A, indicating that perturbations in the N-terminal binding site still allow Rab8 to bind to the C-terminal site, whereas perturbations at Ct-RBS2 also affect binding at Nt-RBS1. This suggests a sequential binding mechanism for Rabs. To further support our observation, we performed SEC experiments with V978A_V985A and V1041A_I1048A bMERB mutants with other Rab8 family members (Rab10, Rab13, and Rab15). Similar observations were made; however, compared to Rab8, Rab10 showed a lesser increase in complex formation upon increasing the bMERB:Rab ratio, suggesting a slightly lower affinity for the N-terminal Rab binding (Supplementary Fig. 7).

The other N-terminal Rab binding site mutant, bMERB$_{M992A_I993A}$, exhibited a similar high affinity for C-terminal Rab8 binding, while a more than 30-fold decrease in N-terminal Rab binding was observed. The residue M992 forms hydrophobic interactions with Y6 of Rab10 (Nt-RBS1) (Fig. 5o, Inset3). An intriguing observation arose with the mutant bMERB$_{L1047A_F1050A}$, which demonstrated reduced binding affinity for both Rab binding sites. This mutant showed over a 20-fold decrease in C-terminal Rab8 binding and a 10-fold reduction in N-terminal Rab binding (Fig. 5p). Residues L1047 and F1050 contribute to hydrophobic interactions with L8 of Rab10 (Nt-RBS1) (Fig. 5c, Inset3). However, L1047 and F1050 do not participate in binding with Rab10 at Ct-RBS2; the decrease in binding affinity might be due to a change in local hydrophobicity, as these residues lie on the opposite side of the crucial I1048. Previously, we reported that the N-terminus of the Rab8 family member provides specificity[28]. L8^{Rab10} is implicated in the RabSF1 interaction with L1047 and F1050, thereby further stabilizing the interaction. These findings suggest that the conformation of helix 3 of the bMERB domain plays a crucial role in Rab binding at both the N-terminal and C-terminal Rab binding sites within the full-length bMERB domain background. This contrasts with our earlier findings, which demonstrated the formation of a stable complex between Rab8 and N- and C-terminal helix-deleted constructs in a 1:1 ratio, implying independence between the Rab binding sites[28]. We suggest that the absence of helix 3 may cause helices 1-2 to adopt a different conformation to accommodate the Rab molecule.

Taken together, our data strongly suggest allosteric communication between both the N-terminal and C-terminal Rab binding sites, with the first Rab molecule binding at Ct-RBS2, followed by the second Rab molecule binding at Nt-RBS1.

The overall structure of the bMERB$_{V978A_V985}$:Rab10/bMERB$_{V978A}$:Rab10 complex

To gain mechanistic insight, we attempted to crystallize bMERB$_{V978A_V985}$:Rab10, bMERB$_{V978A}$:Rab10, bMERB$_{V985A}$:Rab10 complexes, and the bMERB$_{V1041A_I1048A}$ domain. We successfully obtained well-diffracting crystals of the bMERB$_{V978A_V985}$:Rab10 and bMERB$_{V978A}$:Rab10 complexes, with crystals (space group: P 2_1) diffracting to 1.8 and 2.05 Å, respectively. The structures were solved as described in the materials and methods (Data and refinement statistics are shown in Supplementary Table 1).

The asymmetric unit contained a single copy of either the bMERB$_{V978A_V985A}$:Rab10 or bMERB$_{V978A}$:Rab10 complex. Both structures are nearly identical (Fig. 6a and Supplementary Fig. 8**)**, so here we describe the bMERB$_{V978A_V985A}$:Rab10 complex structure in detail. In accordance with our aSEC and ITC data, a single molecule of Rab10 was bound to the C-terminal Rab binding site. Structural alignment of bMERB$_{V978A_V985A}$:Rab10 with the wild-type bMERB:Rab10 (PDB: 5LPN)[28] shows that the C-terminal Rab binding site of the mutant bMERB domain adopts the same conformation as the wild-type complex. However, the second half of helix 2 of the mutant bMERB domain adopts a different

conformation. The N-terminal Rab binding site is formed by a kink in the second half of helix 2 and the movement of the first half of helix 1 towards Rab. In the $bMERB_{V978A_V985A}$:Rab10 structure, the second helix's conformation is similar to the unbound bMERB domain conformation (PDB: 5LEO)[26] (Fig. 6b-c). This mutation of V978 or V985 leads to the abrogation of the second Rab binding at the N-terminal Rab binding site, as found in aSEC/ITC experiments as well.

Phosphomimetic mutation of S960 of the bMERB domain

Recently, Macgarry *et al*., proposed an alternate mode of Mical1 activation by Rho GTPases and showed that upon extracellular ligand stimulation, Cdc42 interacts with its effector PAK1 and active Cdc42:PAK1 then binds to the MO domain of Mical1, PAK1, a serine/threonine kinase, phosphorylates S817 and S960 of the Mical1 bMERB domain[43]. The authors suggest that this phosphorylation leads to an increase in Rab10 binding, which then activates Mical1, resulting in increased F-actin disassembly[43]. We attempted to purify the full-length $Mical1_{S817D_S960D}$ double phosphomimetic mutants but could not achieve adequate purity. We proceeded to analyze our AlphaFold2 model. Despite the low pLDDT score of this region, as it sits in a linker region, the position of this linker in all models is extremely reproducible. The charge repulsion following phosphorylation could potentially induce a 'loosening' of the auto-inhibited complex (Fig. 7a-b and Supplementary Fig. 9). Nevertheless, further biochemical and structural data are required to validate this finding.

Previously, we demonstrated that in addition to Rab8, the bMERB domain interacts with Rab10, Rab13, and Rab15; however, quantitative analysis of the binding affinities was lacking. We have now quantified these interactions, and similar to Rab8, ITC data reveal that Rab10 and Rab15 bind to the bMERB domain in a 1:2 stoichiometry. This binding involves one high-affinity Ct-RBS2 (11 nM for Rab10, 2.5 nM for Rab15; enthalpy-driven) and one low-affinity Nt-RBS1 (3.73 µM for Rab10, 2.91 µM for Rab15; entropy-driven). We then purified the isolated $bMERB_{S960D}$ mutant and assessed its complex formation with the Rab8/Rab10/Rab15 domain through aSEC/ITC experiments. We observed no effect of phosphomimetic mutations in the bMERB domain on Rab interaction. This result aligns with our structural observations. S960 is located in helix 1 of the Nt-RBS1 site and does not participate in binding with Rab10; therefore, we suggest that the phosphorylation of this residue does not affect Rab10 binding (Fig. 7c-o).

Based on our findings and observations, we propose that in the context of activation by PAK1, phosphorylation of both S817 and S960 may facilitate the release of auto-inhibition, thereby exposing the Mical1 domains and enabling the bMERB domain to be more accessible for Rab binding without altering the Rab affinity. However, detailed biochemical data are required to fully understand the activation of Mical1 by the RhoGTPase-PAK1 pathway.

Impact of Rab binding site mutations in the bMERB domain on MO-CH-LIM interaction

In the absence of Rab, the Nt-RBS1 of bMERB accommodates the CH and LIM domain, so we investigated the effect of several RBS mutants of the bMERB domain on MO-CH-LIM interaction (Fig. 8). The L956S mutant displayed more than a 9-fold reduction in binding affinity (Fig. 8c). L956 forms a hydrophobic interaction with L598 of the CH domain; however, it is also part of a continuous array of hydrophobic residues. Therefore, we propose that this mutation may lead to the destabilization of the hydrophobic patch. In contrast, the phosphomimetic mutant S960D did not affect MO-CH-LIM binding, as this residue is not part of the predicted binding interface (Fig. 8d). Another putatively non-interacting residue, the W970A mutant, exhibited a 4-fold decrease in binding affinity (Fig. 8e). Although $W970^{bMERB}$ is not directly involved in the interaction, it may contribute to stabilizing the hydrophobic patch of the bMERB domain, which is crucial for MO-CH-LIM interaction.

The double alanine mutations of V978A_V985A result in a complete loss of interaction with the MO-CH-LIM (Fig. 8f). Interestingly, a single mutation of V978A only leads to a 2-fold reduction in binding affinity (Fig. 8g), while the V985A mutant results in a 10-fold reduction (Fig. 8h). V978 forms a hydrophobic interaction with A602 of the CH domain and with L707 of the LIM domain, whereas V985 interacts hydrophobically with V632 of the $Helix^{CHL}$. This suggests that the hydrophobic nature of the region plays a crucial role in stabilizing the CH and LIM interaction with the bMERB domain. Furthermore, double alanine mutations of other non-interface residues, V1041A_I1048A, exhibit slightly better affinity compared to the wild type (Fig. 8i).

Structural basis of Mical1 activation

To unravel the structural basis for the release of the MO, CH, and LIM domains from the bMERB domain upon Rab binding, we superimposed the Mical1 auto-inhibited AlphaFold2 model with that of the bMERB:Rab10 (PDB: 5LPN) structure[28]. The superimposition clearly shows that in the auto-inhibited Mical1 model, the Nt-RBS1 site is occupied by the CH and LIM domains, along with $Helix^{CHL}$. There is a distinct change in the conformation of the bMERB domain helices upon Rab binding (Fig. 9a-c). Helix 3 of the bMERB domain adopts a defined conformation in the presence of Rab8 (Ct-RBS2), which spatially infringes on the CH domain and $Helix^{CHL}$. Meanwhile, in the presence of the second Rab molecule, helices 1-2 move towards the Rab molecule, and this conformation also sterically hinders interaction with the CH domain.

The AlphaFold2 auto-inhibited model suggests that although the active site is still accessible, helix 1 of the bMERB domain restricts the movement of the catalytic loop (amino acids 395 to 405) (Fig. 3e). Conformational changes of W400 stabilize FAD binding through π-π stacking and could be involved in the transfer of a hydride from NADPH to FAD[40]. Several studies have proposed that during the

oxidation process, methionine residues come close to W400, making them accessible to hydrogen peroxide[40,44]. The AlphaFold2 model clearly shows that enzyme activity most likely would be inhibited by the bMERB domain, by restricting the movement of the catalytic loop (Fig. 3e). Specifically, the movement of F399 is restricted in the Mical1 auto-inhibited model, and the MO domain conformation is similar to that of the isolated MO domain in the oxidized state (PDB: 2BRY) (Fig. 3e).

Next, we propose a model of Mical1 activation (Fig. 10). Structural comparison of the Mical1 auto-inhibited state with the bMERB:Rab10 complex clearly shows that Nt-RBS1 is blocked by CH, Helix^{CHL}, and the LIM domain, whereas helix 3 of the bMERB domain is accessible, and the first Rab8 molecule binds at the C-terminal high-affinity Rab binding site, leading to a defined helix 3 conformation. The movement of helix 3 results in the displacement of the CH domain and Helix^{CHL}. This displacement loosens up the CH, LIM, and Helix^{CHL}, leading to the opening of the structure. The displacement of the CH domain exposes the Nt-RBS1, and a second Rab molecule binds at this low-affinity RBS. This interaction prevents the reassembly of the bMERB:CH:LIM domain. The binding of the second Rab molecule leads to a significant change in the conformation of helix 2 and a small but notable change in the conformation of helix 1. These changes in helices 1 and 2 result in the loss of interaction with the MO domain. The key MO binding interface residues in helices 1 and 2 exhibit different side chain orientations in the Rab-bound structure, particularly the crucial E939, F925, and N999 residues, which leads to the dissociation of the MO domain (Fig. 9d). This observation is supported by our ITC data. Movements of helices 1 and 2 also cause further dissociation of the LIM domain. The binding of the second Rab molecule relieves auto-inhibition, enabling accessibility to the MO, CH, and LIM domains. Subsequently, the active MO domain induces F-actin depolymerization.

Mical1 regulates actin dynamics by selectively oxidizing the Met44 and Met47 of F-actin, in an NADPH-dependent manner[6,45,46]. Met44 and Met47 lie in the DNase-binding loop (D-loop) of actin, which is essential for forming contacts between actin subunits in F-actin and is crucial for filament stability[47,48]. Oxidation of Met44 and Met47 loosens the subunit interaction and destabilizes the F-actin, leading to depolymerization and severing of F-actin[6,49]. We have previously shown that Mical1's CH, LIM, or CH-LIM domain fails to interact with F-actin[30]. The Mical1 CH domain is structurally similar to CH type-2 domains, which are usually present in actin-binding proteins, but cannot bind to F-actin directly. On the other hand, CH type-1 domains can directly bind to F-actin, explaining why the Mical1 CH domain does not interact with F-actin. In the current work, we checked the interaction of F-actin with full-length Mical1, MO-CH-LIM, MO-CH, and MO constructs (Fig. 9e). Using actin co-sedimentation assays, we demonstrated that MO-CH-LIM, MO-CH, and MO constructs can interact with F-actin, suggesting that the MO domain is essential and sufficient for F-actin interaction. We also observed that, compared to the isolated MO-CH-LIM, MO-CH, and MO constructs, full-length Mical1 shows

significantly less interaction with F-actin. This suggests that in the auto-inhibited state, Mical1 fails to interact with F-actin, and the binding of Rab is needed to overcome this auto-inhibition. However, a detailed study is required to show how the MO domain interacts with F-actin, and detailed structural data is required to shed light on the Mical1 and F-actin interaction.

Previously, we suggested that the binding of two Rab molecules to Mical1 could increase the local concentration of specific Rab molecules, thereby creating Rab microdomains. This synergistic binding of two Rab molecules controls Mical1 activity. Based on our data, we now propose that the initial binding of the first Rab molecule to a high-affinity site may facilitate the recruitment of Mical1 to specific membranes and alleviate its auto-inhibited state. Subsequently, this facilitates the binding of the second Rab molecule at a low-affinity Nt-RBS1 site, further stabilizing the active state of Mical1 by blocking the rebinding of the MO, CH, and LIM domains. This process determines the duration of enzyme activity, thereby regulating F-actin dynamics (Fig. 10). For Mical-like proteins, a concerted Rab recruitment cascade has been reported. For instance, Mical-L1 connects Rab35 and Rab8. In another study, it was demonstrated that Mical-L1 is recruited to recycling endosomes by Rab35, subsequently recruiting other Rab proteins such as Rab8, Rab13, and Rab36[50]. Similarly, in the case of Mical1-L2-dependent GLUT4 translocation, trafficking was dependent on the concerted action of Rab8 and Rab13[51]. The authors suggested that bMERB domain dimerization allows for concerted recruitment; however, in the case of Mical1, a single bMERB domain can recruit Rab proteins in a concerted manner.

In conclusion, our study has provided biochemical and structural insights into both the auto-inhibited state and the active state of Mical1. Our data offer a detailed overview of the MO-CH-LIM:bMERB interaction and mutagenesis experiments shed light on the crucial residues involved in this interaction. Furthermore, we have provided insight into the activation mechanism of Mical1 and presented evidence suggesting allosteric regulation between the two Rab binding sites, as well as determining the crucial residues required for Rab recruitment.

Methods

Plasmid cloning

All expression constructs were generated by standard cloning techniques, using Phusion polymerase, restriction digestion, and ligation by T4 DNA ligase, and point mutants were generated by quick-change site-directed mutagenesis, using Phusion polymerase. All plasmids were verified by Sanger sequencing. The bacterial expression constructs for Mical1, MO-CH-LIM, MO-CH, and MO were

previously described[52]. A detailed overview of all expression vectors employed in this study is presented in Supplementary Table 2.

Recombinant protein expression and purification

Human Mical1 full-length and truncated C-terminal His6-tagged versions of MO, MO-CH, and MO-CH-LIM domains were expressed and purified with a modified protocol as described previously[52]. Proteins were recombinantly expressed in *E. coli* Rosetta (DE3) (Merck Millipore) cells in LB media supplemented with Ampicillin (125 µg/mL) and Chloramphenicol (34 µg/mL) and cells were grown at 37°C to OD_{600} nm = 0.8–1.0 and stored at 4°C for 30 min. Expression was induced by the addition of 0.5 mM IPTG, and cells were allowed to grow at 19°C for 14-16 hr. Cells were pelleted and stored at -80°C until ready for purification. Cells were mechanically lysed by passing through a fluidizer (Microfluidic**)** in a buffer [Buffer A: 50 mM Hepes pH 8.0, 500 mM NaCl, 2 mM βME (2-Mercaptoethanol), 1 mM PMSF (Phenylmethylsulfonyl fluoride) and 1 mM CHAPS (3-((3-cholamidopropyl) dimethylammonio)-1-propanesulfonate)] and lysates were cleared by centrifugation at 75,600 g at 4 °C for 30 min using a JA 25.50 rotor (Beckman-Coulter). Next, the proteins were purified by Ni^{2+}-affinity chromatography, and protein fractions were eluted with an imidazole gradient (Buffer B: buffer A supplemented with 500 mM imidazole pH 8.0). The His6-tagged protein was overnight dialyzed at 4 °C in a buffer (50 mM Tris pH 8.0, 100 mM NaCl, and 2 mM βME). Further purity was achieved by gel filtration (HiLoad Superdex 200 26/60, GE Healthcare) (Buffer: 20 mM Tris 8.0, 100 mM NaCl, and 2 mM DTE). Depending on purity, the protein was further purified by one to three successive rounds of anion exchange chromatography (POROS™ 50 HQ strong anion exchange resin; Thermo Scientific™). The purified protein was collected, concentrated, and washed with final buffer (Storage buffer: 20 mM Tris pH 8.0, 100 mM NaCl, and 2 mM DTE) using Amicon® Ultra-15 50K NMWL centrifugal filter devices; flash-frozen in liquid N_2 and stored at −80 °C. Protein concentration was determined by using Bradford assay (Bio-Rad). Tag-free Mical1 full-length bMERB domain, truncated bMERB domains, and mutants were purified as described previously[28].

Human Rab GTPases (tag-free) were expressed and purified as described previously[28]. Rabs were preparatively loaded with GppNHp (Guanosine-5'-[β-γ-Imido]-triphosphate) and the reaction was performed as described previously [28]. Nucleotide exchange efficiency was quantified by C18 reversed-phase column (Prontosil C18, Bischoff Chromatography) with HPLC in 50 mM potassium phosphate buffer pH 6.6, 10 mM tetrabutylammonium bromide and 12% acetonitrile (v/v). Protein samples were heat precipitated at 95 °C for 5 min and centrifuged at 15700 g for 10 min and loaded (25 µM, 20 µL) on the column. Peaks were integrated and to determine the nucleotide retention times; a nucleotide

standard run was performed. The purified protein was collected and concentrated; flash-frozen in liquid N_2 and stored at −80 °C.

Size exclusion chromatography coupled with multi-angle light scattering (SEC-MALS)

Full-length Mical1, MO-CH-LIM, MO-CH, and MO domains were analyzed using a Superdex 200 10/30 GL column coupled with a multi-angle light scattering (MALS) instrument (Wyatt Technology). The analysis was conducted in a buffer containing 20 mM Hepes (pH 8.0), 50 mM NaCl, 1 mM $MgCl_2$, and 1 mM TCEP. The bMERB domain was analyzed using a Superdex 75 10/30 GL column coupled with a multi-angle light scattering (MALS) instrument (Wyatt Technology) in a buffer containing 20 mM Hepes (pH 7.5), 50 mM NaCl, 1 mM $MgCl_2$, and 1 mM TCEP. The chromatography system was connected in series with a light-scattering detector (Wyatt Dawn HELIOS II) and a refractive index detector (Wyatt Optilab t-rEX). BSA (Sigma) was used as a standard to calibrate the system, and 20 µL of each sample (2 mg/mL) was injected. The data analysis was performed with ASTRA 7.3.2 software (Wyatt Technologies), yielding the molar mass and mass distribution (polydispersity) of the samples.

Analytical size exclusion chromatography (aSEC)

The bMERB:GppNHp Rab ($Rab8a_{1-176}$, $Rab10_{1-175}$, $Rab13_{1-176}$, and $Rab15_{1-176}$) complex formation was analyzed by analytical size exclusion chromatography (aSEC). 110 µM of bMERB domain and 121 µM of GppNHp protein (Effector: Rab stoichiometry of 1: 1.1) were mixed in a buffer containing 20 mM Hepes pH 7.5, 50 mM NaCl, 1 mM $MgCl_2$, and 2 mM DTE and centrifuged for 15 min at 15700 g at 4°C. 40 µL of the mixture was injected into a Superdex 75 10/300 GL gel filtration column (GE Healthcare) pre-equilibrated with the Rab buffer with a flow rate of 0.5 mL/min at room temperature and absorption at 280 nm was recorded.

Isothermal titration calorimetry (ITC)

Protein-protein interaction measurements were conducted by isothermal titration calorimetry (ITC) using an ITC200 and PEAQ-ITC microcalorimeter (MicroCal). $Mical1_{fl}$/bMERB:Rab interaction measurements were performed in the buffer containing 20 mM Hepes 7.5, 50 mM NaCl, 1 mM $MgCl_2$, and 1 mM Tris (2-carboxymethyl) phosphine (TCEP) whereas MO-CH-LIM/MO-CH/MO:bMERB interactions were performed in buffer containing 20 mM Hepes 8.0, 150 mM NaCl and 1 mM TCEP at 25°C. Wild types and mutant proteins were dialyzed overnight in their respective buffer. Samples were centrifuged at 15700 g for 30 min at 4°C and protein concentration was determined by Bradford assay (Bio-Rad). 600 µM of GppNHp $Rab8a_{1-176}$ was titrated into the cell containing 30 µM bMERB domain and for full-length Mical1: Rab8 measurement, 800 µM of GppNHp $Rab8a_{1-176}$ was titrated into the cell containing 40 µM full length Mical1. For MO-CH-LIM/MO-CH/MO:bMERB interaction 600 µM of bMERB domain was titrated into the cell containing 30 µM MO-CH-LIM/MO-CH/MO domain. For the

control experiments, the buffer was titrated into the cell containing the protein of interest. In the second control experiment, the protein in the syringe was titrated against the buffer. The binding isotherms were integrated and corrected for the offset by subtracting the control experiment, and the data were fitted to a one-site-binding or two-site-binding model using PEAQ-ITC software. The reported ITC result is representative of one of at least three independent measurements.

AlphaFold2 molecular modeling

The Mical1 models ($Mical1_{fl}$ and MO-CH-LIM:bMERB complex) were generated using AlphaFold multimer v2.3.1[31].

Cross-Linking experiment

Full-length Mical1 (25 µM) was mixed with a 10-fold excess of freshly dissolved DSBU (disuccinimidyl dibutyric urea; Thermo Fisher SCIENTIFIC, 50 mM stock) in DMSO in a cross-linking buffer (20 mM Hepes, 100 mM NaCl, and 2 mM DTE). In a second experiment, 50 µM of MO-CH-LIM (residues 1-781) was mixed with 100 µM of bMERB domain (residues 918-1067) in a final ratio of 1:2, respectively, and again, 10 times DSBU was added in the crosslinking buffer. Samples were incubated at room temperature for 1.30 hours, and the crosslinking reactions were quenched by the addition of 100 mM Tris, pH 8.0. The samples were flash-frozen for further processing, as described previously[53]. Briefly, the processing steps included the reduction of disulfide bonds using tris(2-carboxyethyl) phosphine, alkylation of free thiol groups on cysteines with iodoacetamide, and proteolysis with trypsin. The resulting peptides were enriched as described previously[54]. Briefly, the peptides were fractionated using a Superdex™ 30 Increase 3.2/300 column in a buffer containing 50 mM ammonium acetate, 30% acetonitrile, and 0.1% formic acid. Eluted samples were dried using a centrifugal evaporator and stored at −20 °C until measurement.

LC-MS/MS Analysis

LC-MS/MS analysis was performed as described previously[54]. Briefly, peptides were dissolved in 20 µL of water containing 0.1% TFA. A total of 3 µL of this peptide solution were separated on an Ultimate 3000 RSLC nano system (precolumn: C18, Acclaim PepMap, 300 µm × 5 mm, 5 µm, 100 Å, separation column: C18, Acclaim PepMap, 75 µm × 500 mm, 2 µm, 100 Å, Thermo Fisher Scientific). After loading the sample on the pre-column, a multistep gradient from 5−40% B (90 min), 40−60% B (5 min), and 60−95% B (5 min) was used with a flow rate of 300 nL/min; solvent A: water + 0.1% formic acid; solvent B: acetonitrile + 0.1% formic acid. The nano-HPLC system was coupled to a Q-Exactive Plus mass spectrometer (Thermo Fisher Scientific). Data were acquired in data-dependent MS/MS mode. For full scan MS, we used a mass range of m/z 300−1800, resolution of R = 140000 at m/z 200, one microscan using an automated gain control (AGC) target of 3e6, and a maximum injection time (IT) of 50 ms.

Then, we acquired up to 10 HCD MS/MS scans of the most intense at least doubly charged ions (resolution 17500, AGC target 1e5, IT 100 ms, isolation window 4.0 m/z, normalized collision energy 25.0, intensity threshold 2e4, dynamic exclusion 20.0 s). All spectra were recorded in profile mode.

Data Analysis and Cross-link Identification.

Raw data from the Q-Exactive were converted to MGF (Mascot generic files) format with the program msConvert GUI from ProteoWizard Toolkit version 3[55] and the mgf-files of all fractions of a crosslink were merged into one file. Program MeroX version 2.0.1.4[56,57] was used for cross-link identification. MS data in MGF format and protein sequences in FASTA format were loaded on the program and the cross-linked residues were searched. In the settings, the precursor precision and the fragment ion precision were set to 10.0 and 20.0 ppm, respectively. MS1 data were re-calibrated by 5 ppm according to the average mass deviation of the raw MS data. The FDR was set to 50, i.e. no filtering according to FDR with MeroX was done. RISEUP mode was used, and the maximum missing ions was set to 1. Crosslinks data were exported to XiViewer[58].

Crystallization and structure determination

Initial crystallization condition screens for the protein complexes described in the paper were performed using the JSG CORE I-IV, Pact, and Protein Complex suites (Qiagen). The sitting-drop vapor diffusion method was employed, with a reservoir volume of 70 µL and a drop volume of 0.1 µL for the protein (300 µM complexes, 1:1 Rab:effector) and 0.1 µL for the reservoir solution at 20°C. The best conditions were then optimized using the sitting-drop vapor diffusion method, with varying drop sizes, to obtain well-diffracting crystals. The complex of $bMERB_{V978A_V985A}$:$Rab10_{1-175}$ (300 µM of 1:1 complex) was crystallized in 0.17 M Sodium acetate, 0.085 M Tris-HCl pH 8.5, 25.5% (w/v) PEG 4000 and 15% (v/v) glycerol. The complex $bMERB_{V978A}$:$Rab10_{1-175}$ (300 µM of 1:1 complex) was crystallized in 0.1 M Imidazole pH 8.0, 5% (w/v) PEG 3000 and 30% (v/v) PEG 200. Crystals were fished directly from the crystallization drop and flash-cooled in liquid nitrogen. Diffraction data of $bMERB_{V978A_V985A}$:$Rab10_{1-175}$ was collected at 100 K on beamline X10SA at the Swiss Light Source (Paul Scherrer Institute, Villigen, Switzerland). For the $bMERB_{V978A_V985A}$:$Rab10_{1-175}$ complex crystal, a native data set was collected at a wavelength of 0.999968 Å. Whereas diffraction data of $bMERB_{V978A}$:$Rab10_{1-175}$ was collected at 100 K on beamline ID23-2 at the European Synchrotron Radiation Facility (Grenoble, France). For the $bMERB_{V978A}$:$Rab10_{1-175}$ complex crystal, a native data set was collected at a wavelength of 0.873130 Å. Data were integrated and scaled with XDS[59].

The crystal of the $bMERB_{V978A_V985A}$:$Rab10_{1-175}$ complex diffracted to a resolution of 1.8 Å (space group $P2_1$ with a = 53.673 Å, b = 48.807 Å, c = 79.199 Å), and a single copy of the complex is present in the asymmetric unit of the crystal. The initial model for the $bMERB_{V978A_V985A}$:$Rab10_{1-175}$ complex was

obtained by molecular replacement using PHASER[60] with the crystal structure of the Mical1$_{bMERB}$:Rab 10 (PDB: 5LPN) as a search model[28]. The partial model was completed by manual building in Coot[61]. For the bMERB$_{V978A}$:Rab10$_{1-175}$ complex, the crystal diffracted to a resolution of 2.05 Å (space group $P2_1$ with a = 53.517 Å, b = 49.434 Å, c = 79.095 Å), and one copy of the complex constitutes the asymmetric unit of the crystal. The partial model was obtained by molecular replacement using PHASER[60] and the bMERB$_{V978A_V985A}$:Rab10$_{1-175}$ was used as a search model. The initial model was completed by manual building in Coot[61]. The final models were refined to convergence with phenix.refine[62].

Data collection and refinement statistics are summarized in Supplementary Table 1. Structural figures were prepared using PyMOL (DeLano Scientific; http://www.pymol.org).

Actin co-sedimentation assay

Rabbit skeletal muscle G-actin (AKL99) was purchased from Cytoskeleton. Inc and polymerized into F-actin according to the manufacturer's protocol. F-actin (10 µM) was incubated for 1 hr at room temperature (RT) with MO/MO-CH/MO-CH-LIM/Mical1$_{fl}$ (10 µM) in a buffer containing 20 mM Hepes (pH 8.0), 50 mM KCl, 2 mM $MgCl_2$, 1 mM DTT, and 2 mM NaN_3. Samples were centrifuged at 100,000 g for 1 hr at 4°C. The supernatant and pellet were subjected to 4-15% gradient SDS-PAGE, followed by Coomassie Brilliant Blue staining.

Bioinformatics

Multiple sequence alignments were generated using Clustal Omega[63]. The protein interaction interfaces from the asymmetric unit were examined in detail using the PDBePISA server (Proteins, Interfaces, Structures, and Assemblies)[64]. The DALI server was used for structural comparison[65].

Data availability

The plasmids generated in this study are available from the corresponding author upon request. Protein coordinates and structure factors have been submitted to the Protein Data Bank under accession codes.

PDB: XXX (bMERB$_{V978A_V985A}$:Rab10)

PDB: XXX (bMERB$_{V978A}$:Rab10)

Source data are provided with this paper.

References

1. Blanchoin, L., Boujemaa-Paterski, R., Sykes, C. & Plastino, J. Actin dynamics, architecture, and mechanics in cell motility. *Physiol Rev* **94**, 235-63 (2014).
2. Pollard, T.D. Actin and Actin-Binding Proteins. *Cold Spring Harb Perspect Biol* **8**(2016).
3. Lappalainen, P., Kotila, T., Jegou, A. & Romet-Lemonne, G. Biochemical and mechanical regulation of actin dynamics. *Nat Rev Mol Cell Biol* **23**, 836-852 (2022).
4. Varland, S., Vandekerckhove, J. & Drazic, A. Actin Post-translational Modifications: The Cinderella of Cytoskeletal Control. *Trends Biochem Sci* **44**, 502-516 (2019).
5. Terman, J.R., Mao, T., Pasterkamp, R.J., Yu, H.H. & Kolodkin, A.L. MICALs, a family of conserved flavoprotein oxidoreductases, function in plexin-mediated axonal repulsion. *Cell* **109**, 887-900 (2002).
6. Hung, R.J., Pak, C.W. & Terman, J.R. Direct redox regulation of F-actin assembly and disassembly by Mical. *Science* **334**, 1710-3 (2011).
7. Hung, R.J., Spaeth, C.S., Yesilyurt, H.G. & Terman, J.R. SelR reverses Mical-mediated oxidation of actin to regulate F-actin dynamics. *Nat Cell Biol* **15**, 1445-54 (2013).
8. Lee, B.C. et al. MsrB1 and MICALs regulate actin assembly and macrophage function via reversible stereoselective methionine oxidation. *Mol Cell* **51**, 397-404 (2013).
9. Rajan, S., Terman, J.R. & Reisler, E. MICAL-mediated oxidation of actin and its effects on cytoskeletal and cellular dynamics. *Front Cell Dev Biol* **11**, 1124202 (2023).
10. Cai, K. et al. MICAL1 facilitates pancreatic cancer proliferation, migration, and invasion by activating WNT/beta-catenin pathway. *J Transl Med* **20**, 528 (2022).
11. Deng, W. et al. MICAL1 controls cell invasive phenotype via regulating oxidative stress in breast cancer cells. *BMC Cancer* **16**, 489 (2016).
12. Zhao, S. et al. NEDD9 Facilitates Hypoxia-Induced Gastric Cancer Cell Migration via MICAL1 Related Rac1 Activation. *Front Pharmacol* **10**, 291 (2019).
13. Gu, H. et al. MICAL1 inhibits colorectal cancer cell migration and proliferation by regulating the EGR1/beta-catenin signaling pathway. *Biochem Pharmacol* **195**, 114870 (2022).
14. Loria, R. et al. Sema6A and Mical1 control cell growth and survival of BRAFV600E human melanoma cells. *Oncotarget* **6**, 2779-93 (2015).
15. Prifti, E. et al. Mical modulates Tau toxicity via cysteine oxidation in vivo. *Acta Neuropathol Commun* **10**, 44 (2022).
16. Xu, C. et al. MICAL1 (molecule interacting with CasL 1) protects oligodendrocyte cells from oxidative injury through regulating apoptosis, autophagy in spinal cord injury. *Neurosci Lett* **750**, 135712 (2021).
17. Dazzo, E. et al. Mutations in MICAL-1cause autosomal-dominant lateral temporal epilepsy. *Ann Neurol* **83**, 483-493 (2018).
18. Alto, L.T. & Terman, J.R. MICALs. *Curr Biol* **28**, R538-R541 (2018).
19. Suzuki, T. et al. MICAL, a novel CasL interacting molecule, associates with vimentin. *J Biol Chem* **277**, 14933-41 (2002).
20. Van Battum, E.Y. et al. The intracellular redox protein MICAL-1 regulates the development of hippocampal mossy fibre connections. *Nat Commun* **5**, 4317 (2014).
21. Fremont, S., Romet-Lemonne, G., Houdusse, A. & Echard, A. Emerging roles of MICAL family proteins - from actin oxidation to membrane trafficking during cytokinesis. *J Cell Sci* **130**, 1509-1517 (2017).
22. Stenmark, H. Rab GTPases as coordinators of vesicle traffic. *Nat Rev Mol Cell Biol* **10**, 513-25 (2009).
23. Barr, F. & Lambright, D.G. Rab GEFs and GAPs. *Curr Opin Cell Biol* **22**, 461-70 (2010).
24. Muller, M.P. & Goody, R.S. Molecular control of Rab activity by GEFs, GAPs and GDI. *Small GTPases* **9**, 5-21 (2018).
25. Lamber, E.P., Siedenburg, A.C. & Barr, F.A. Rab regulation by GEFs and GAPs during membrane traffic. *Curr Opin Cell Biol* **59**, 34-39 (2019).

26. Fremont, S. et al. Oxidation of F-actin controls the terminal steps of cytokinesis. *Nat Commun* **8**, 14528 (2017).
27. Esposito, A. et al. Human MICAL1: Activation by the small GTPase Rab8 and small-angle X-ray scattering studies on the oligomerization state of MICAL1 and its complex with Rab8. *Protein Sci* **28**, 150-166 (2019).
28. Rai, A. et al. bMERB domains are bivalent Rab8 family effectors evolved by gene duplication. *Elife* **5**(2016).
29. Rai, A., Goody, R.S. & Muller, M.P. Multivalency in Rab effector interactions. *Small GTPases* **10**, 40-46 (2019).
30. Rai, A., Bleimling, N., Vetter, I.R. & Goody, R.S. The mechanism of activation of the actin binding protein EHBP1 by Rab8 family members. *Nat Commun* **11**, 4187 (2020).
31. Jumper, J. et al. Highly accurate protein structure prediction with AlphaFold. *Nature* **596**, 583-589 (2021).
32. Abou-Zeid, N. et al. MICAL-like1 mediates epidermal growth factor receptor endocytosis. *Mol Biol Cell* **22**, 3431-41 (2011).
33. Sakane, A. et al. Rab13 small G protein and junctional Rab13-binding protein (JRAB) orchestrate actin cytoskeletal organization during epithelial junctional development. *J Biol Chem* **287**, 42455-68 (2012).
34. Miyake, K. et al. Actin Cytoskeletal Reorganization Function of JRAB/MICAL-L2 Is Fine-tuned by Intramolecular Interaction between First LIM Zinc Finger and C-terminal Coiled-coil Domains. *Sci Rep* **9**, 12794 (2019).
35. Sakane, A. et al. Conformational plasticity of JRAB/MICAL-L2 provides "law and order" in collective cell migration. *Mol Biol Cell* **27**, 3095-3108 (2016).
36. Schmidt, E.F., Shim, S.O. & Strittmatter, S.M. Release of MICAL autoinhibition by semaphorin-plexin signaling promotes interaction with collapsin response mediator protein. *J Neurosci* **28**, 2287-97 (2008).
37. Giridharan, S.S. & Caplan, S. MICAL-family proteins: Complex regulators of the actin cytoskeleton. *Antioxid Redox Signal* **20**, 2059-73 (2014).
38. Zhang, N., Yao, L.L. & Li, X.D. Regulation of class V myosin. *Cell Mol Life Sci* **75**, 261-273 (2018).
39. Kelley, C.F. et al. Phosphoinositides regulate force-independent interactions between talin, vinculin, and actin. *Elife* **9**(2020).
40. Siebold, C. et al. High-resolution structure of the catalytic region of MICAL (molecule interacting with CasL), a multidomain flavoenzyme-signaling molecule. *Proc Natl Acad Sci U S A* **102**, 16836-41 (2005).
41. Sun, H. et al. Solution structure of calponin homology domain of Human MICAL-1. *J Biomol NMR* **36**, 295-300 (2006).
42. Sato, M. et al. Solution structures of the LIM domain of human NEDD9 interacting protein with calponin homology and LIM domains. (RIKEN Structural Genomics/Proteomics Initiative (RSGI), 2005).
43. McGarry, D.J. et al. MICAL1 activation by PAK1 mediates actin filament disassembly. *Cell Rep* **41**, 111442 (2022).
44. Manta, B. & Gladyshev, V.N. Regulated methionine oxidation by monooxygenases. *Free Radic Biol Med* **109**, 141-155 (2017).
45. Wu, H., Yesilyurt, H.G., Yoon, J. & Terman, J.R. The MICALs are a Family of F-actin Dismantling Oxidoreductases Conserved from Drosophila to Humans. *Sci Rep* **8**, 937 (2018).
46. Zucchini, D., Caprini, G., Pasterkamp, R.J., Tedeschi, G. & Vanoni, M.A. Kinetic and spectroscopic characterization of the putative monooxygenase domain of human MICAL-1. *Arch Biochem Biophys* **515**, 1-13 (2011).
47. Oztug Durer, Z.A., Diraviyam, K., Sept, D., Kudryashov, D.S. & Reisler, E. F-actin structure destabilization and DNase I binding loop: fluctuations mutational cross-linking and electron microscopy analysis of loop states and effects on F-actin. *J Mol Biol* **395**, 544-57 (2010).

48. Das, S. et al. D-loop Dynamics and Near-Atomic-Resolution Cryo-EM Structure of Phalloidin-Bound F-Actin. *Structure* **28**, 586-593 e3 (2020).
49. Grintsevich, E.E. et al. Catastrophic disassembly of actin filaments via Mical-mediated oxidation. *Nat Commun* **8**, 2183 (2017).
50. Kobayashi, H., Etoh, K., Ohbayashi, N. & Fukuda, M. Rab35 promotes the recruitment of Rab8, Rab13 and Rab36 to recycling endosomes through MICAL-L1 during neurite outgrowth. *Biol Open* **3**, 803-14 (2014).
51. Sun, Y., Bilan, P.J., Liu, Z. & Klip, A. Rab8A and Rab13 are activated by insulin and regulate GLUT4 translocation in muscle cells. *Proc Natl Acad Sci U S A* **107**, 19909-14 (2010).
52. Vitali, T., Maffioli, E., Tedeschi, G. & Vanoni, M.A. Properties and catalytic activities of MICAL1, the flavoenzyme involved in cytoskeleton dynamics, and modulation by its CH, LIM and C-terminal domains. *Arch Biochem Biophys* **593**, 24-37 (2016).
53. Koch, D. et al. A pull-down procedure for the identification of unknown GEFs for small GTPases. *Small GTPases* **7**, 93-106 (2016).
54. Pan, D., Brockmeyer, A., Mueller, F., Musacchio, A. & Bange, T. Simplified Protocol for Cross-linking Mass Spectrometry Using the MS-Cleavable Cross-linker DSBU with Efficient Cross-link Identification. *Anal Chem* **90**, 10990-10999 (2018).
55. Chambers, M.C. et al. A cross-platform toolkit for mass spectrometry and proteomics. *Nat Biotechnol* **30**, 918-20 (2012).
56. Arlt, C. et al. Integrated Workflow for Structural Proteomics Studies Based on Cross-Linking/Mass Spectrometry with an MS/MS Cleavable Cross-Linker. *Anal Chem* **88**, 7930-7 (2016).
57. Gotze, M. et al. Automated assignment of MS/MS cleavable cross-links in protein 3D-structure analysis. *J Am Soc Mass Spectrom* **26**, 83-97 (2015).
58. Graham, M., Combe, C., Kolbowski, L. & Rappsilber, J. xiView: A common platform for the downstream analysis of Crosslinking Mass Spectrometry data. *bioRxiv* (2019).
59. Kabsch, W. Xds. *Acta Crystallogr D Biol Crystallogr* **66**, 125-32 (2010).
60. McCoy, A.J. et al. Phaser crystallographic software. *J Appl Crystallogr* **40**, 658-674 (2007).
61. Emsley, P., Lohkamp, B., Scott, W.G. & Cowtan, K. Features and development of Coot. *Acta Crystallogr D Biol Crystallogr* **66**, 486-501 (2010).
62. Adams, P.D. et al. PHENIX: a comprehensive Python-based system for macromolecular structure solution. *Acta Crystallogr D Biol Crystallogr* **66**, 213-21 (2010).
63. Sievers, F. et al. Fast, scalable generation of high-quality protein multiple sequence alignments using Clustal Omega. *Mol Syst Biol* **7**, 539 (2011).
64. Krissinel, E. & Henrick, K. Inference of macromolecular assemblies from crystalline state. *J Mol Biol* **372**, 774-97 (2007).
65. Holm, L. Benchmarking fold detection by DaliLite v.5. *Bioinformatics* **35**, 5326-5327 (2019).

Acknowledgments

We are grateful to Prof. Maria Vanoni for sharing the full-length Mical1, MO-CH-LIM, MO-CH, and MO bacterial expression constructs and providing the purification protocol. We also thank the beamline staff of the Swiss Light Source (SLS) X10SA at the Paul Scherrer Institute, Villigen, Switzerland, and the beamline staff of the European Synchrotron Radiation Facility at Grenoble, France, for their assistance during data collection. We thank Dr. Raphael Gasper and Dr. Matthias Müller for the X-ray diffraction data collection. We express our gratitude to Petra Geue for conducting the SEC-MALS measurements

and data analysis. Special thanks are extended to Franziska Müller for her contributions to the size exclusion chromatography experiment for the peptides. We are thankful to Malte Metz and Andreas Brockmeyer for conducting the LC-MS/MS runs and method setup. Additionally, we acknowledge financial support from the Max-Planck-Society and the Deutsche Forschungsgemeinschaft (grant GO 284/10-1 to R.S.G).

Author contributions

A.R. conceived and designed the study, carried out protein expression and purification, conducted all biochemical studies, cross-linking experiments, crystallization, and determined X-ray structures. P.J. performed LC-MS/MS experiments, conducted data analysis, and identified cross-links. I.R.V. conducted Mical1 AlphaFold2 modeling and analyzed the structure. R.S.G. acquired funding. A.R., P.J., I.R.V., and R.S.G. analyzed and interpreted the data. A.R. wrote the manuscript with critical input from all authors.

Competing interests

The authors declare no competing interest.

Figure Legends

Fig. 1: Mical1 MO-CH-LIM domains form an intramolecular complex with its bMERB domain. a A schematic diagram of human Mical1: Mical1 contains an N-terminal monooxygenase (MO) domain, calponin homology (CH) domain, Lin11, Isl-1, and Mec-3 (LIM) domain, and a C-terminal coiled-coil bMERB (bivalent Mical/EHBP Rab binding) domain. PRM: proline-rich motif. **b-f** Size exclusion chromatography (Superdex 200) coupled with multi-angle light scattering (SEC-MALS) was performed for full-length Mical1, MO-CH-LIM, MO-CH, and MO, while size exclusion chromatography (Superdex 75) coupled with SEC-MALS was conducted for the bMERB domain. The Rayleigh scattering is represented in blue, and the molecular weight distribution across the peak is shown in gray. The measured molecular weight closely corresponds to that of a monomer. **g-i** MO-CH-LIM domain construct interacts with the bMERB domain. Binding affinities were measured by titrating the bMERB domain (600 µM) with the MO-CH-LIM/MO-CH/MO domain (40 µM). Integrated heat peaks, corrected for the offset by subtracting the control experiment, were fitted to a one-site-binding model, yielding the binding stoichiometry (N), enthalpy (ΔH), entropy (ΔS), and dissociation constant (K_D). Clear complex formation was observed for the MO-CH-LIM, whereas no complex formation was observed

for the MO-CH and MO. The data represents results from at least three independent experiments. N.D. denotes not detected.

Fig. 2: Full-length bMERB domain is essential for interaction with MO-CH-LIM domains. a-c The full-length bMERB domain is required for MO-CH-LIM interaction. Binding affinities were measured by titrating the bMERB/$bMERB_{H1-2}$/$bMERB_{H2-3}$ domain (600 µM) with the MO-CH-LIM domain (40 µM). Integrated heat peaks, corrected for the offset by subtracting the control experiment, were fitted to a one-site-binding model, yielding the binding stoichiometry (N), enthalpy (ΔH), entropy (ΔS), and dissociation constant (K_D). The data clearly show that the full-length bMERB construct is necessary for interaction with MO-CH-LIM. The data are representative of at least three repetitions. N.D. denotes not detected. **d** The Coomassie blue-stained SDS-PAGE analysis of purified Mical1 and the MO-CH-LIM:bMERB complex proteins, incubated in the absence or presence of the crosslinker disuccinimidyl dibutyric urea (DSBU), demonstrates efficient DSBU-dependent crosslinking. **e-f** Intramolecular crosslinking of Mical1. **e** Schematic visualization showing inter- and intra-domain crosslinks identified by mass spectrometry analysis of purified full-length Mical1 crosslinked by DSBU. Crosslinks are shown in light purple. **f** Schematic diagram showing inter and intra-domain crosslinks between purified MO-CH-LIM and bMERB domain crosslinked by DSBU. Schematic diagram illustrating inter- and intra-domain crosslinks between the purified MO-CH-LIM and bMERB domains, crosslinked by DSBU. Self-crosslinks are shown in light purple, whereas crosslinks between the isolated MO-CH-LIM and bMERB domains are shown in light blue.

Fig. 3: AlphaFold2 model of auto-inhibited Mical1. a The cartoon representation of the AlphaFold2 Mical1 model. The MO domain, CH domain, LIM domain, the helix connecting the CH and LIM domains ($Helix^{CHL}$), and the bMERB domain of Mical1 are colored in orange, pink, blue, gray, and green, respectively. The insets highlight the various binding interfaces between the MO:bMERB, CH:bMERB, LIM:bMERB, and $Helix^{CHL}$:bMERB domains, with hydrogen bonds and salt bridges indicated by gray dashed lines. **b-c** The cartoon representation of the bMERB domain depicts the MO domain, CH domain, LIM domain, and $Helix^{CHL}$ binding interfaces in orange, pink, blue, and gray dashed lines, respectively. The hydrophobic patches are shown in red dashed lines on the bMERB domain. **d** Structural alignment was performed between the oxidized mouse Mical1 MO domain (light orange, PDB: 2BRY) and the reduced mouse Mical1 MO domain (slate, PDB: 2C4C), and both were compared with the human Mical1 AlphaFold2 model (MO domain in orange and bMERB domain in green). **e** Schematic illustration showing the movement of the isoalloxazine ring of the FAD head during the catalytic cycle upon NADPH treatment. Insets depict the conformational changes of several active site residues upon NADPH treatment. **f** Results from a systematic analysis of the binding interfaces between various domains of the AlphaFold2-predicted Mical1 auto-inhibited model using PISA[64].

Fig. 4: Crucial bMERB interface residues for MO-CH-LIM interaction. a Schematic illustration of the interactions between the MO-CH-LIM and the bMERB domain. Hydrophobic interactions are represented by light orange dashed lines, while hydrogen bonds (H-bonds) and salt bridges are depicted with gray dashed lines. Residues that have been mutated are highlighted in red dashed boxes. **b–i** Mutational alanine screening of the bMERB domain via ITC measurements. The binding of different bMERB mutants (600 µM) with MO-CH-LIM (40 µM) was systematically tested and affinities were determined by ITC experiments. Integrated heat peaks, corrected for the offset by subtracting the control experiment, were fitted to a one-site-binding model, yielding the binding stoichiometry (N), enthalpy (ΔH), entropy (ΔS), and dissociation constant (K_D). N.D. denotes not detected. No binding was detected for the mutant F925A or the mutant L1047A_F1050A. However, a more than 5-fold reduction in binding affinity was observed for all other mutants, except for K918A_E921A, which exhibited a marginal defect. The data represent at least three repetitions.

Fig. 5: Allostery between the Rab binding domains. a A schematic diagram of human Mical1. **b** Full length Mical1 binds to Rab8 in 1:2 stoichiometry. Binding affinities were measured by titrating the Rab8 (800 µM) to full-length Mical1 (40 µM). Integrated heat peaks were fitted to a two-site-binding model yielding the binding stoichiometry (N), the enthalpy (ΔH), the entropy (ΔS), and the dissociation constant (K_D). **b** Cartoon representation of the bMERB:Rab10 complex structure (PDB: 5LPN)[28], with the bMERB domain colored in green and the Rab10 domain in wheat. **c-d** Schematic illustration of the interactions between the bMERB domain and Rab10. Rab10 binds to the Mical1 bMERB domain via its N-terminal regions, switch regions, and inter-switch region. Hydrogen bonds and salt bridges are depicted with gray dashed lines, while light orange dashed lines indicate hydrophobic interactions. RabSF1, RabSF2, RabF1, RabF2, RabF3, and RabF4 motifs are colored in orange, gray, green, pink, purple, and brown, respectively. Additionally, analytical size exclusion chromatography results are provided from a systematic analysis of interactions between the bMERB domain mutants and increasing concentrations of Rab8 (refer to Supplementary Fig. 4 and 5). **e-g, m-n** The bMERB domain (green), Rab8 (gray), and a mixture of both (blue) were loaded onto a Superdex 75 10/300 GL column to monitor for complex formation. **h-l, o-p** Binding affinities were measured by titrating the Rab8 (600 µM) to mutants bMERB domain (30 µM). Integrated heat peaks were fitted to a one-site-binding or two-site-binding model yielding the binding stoichiometry (N), the enthalpy (ΔH), the entropy (ΔS), and the dissociation constant (K_D). The data are representative of at least three repetitions.

Fig. 6: Crystal structure of the bMERB$_{V978A_V985A}$:Rab10 complex. a Cartoon depiction of the bMERB$_{V978A_V985A}$:Rab10 complex. A single Rab10 molecule (gray) binds to the bMERB$_{V978A_V985A}$ domain (blue) at the high-affinity C-terminal Rab-binding site. Switch I and Switch II of Rab10 are shown in red and blue, respectively. GppNHp and Mg^{2+} are depicted as sticks and a green sphere, respectively. **b**

Structural superposition of the $bMERB_{V978A_V985A}$:Rab10 complex and bMERB:Rab10 complex (PDB: 5LPN)[28]. **c** Structural alignment of the bMERB domains of $bMERB_{V978A_V985A}$:Rab10 (blue) with the bMERB:Rab10 (PDB: 5LPN)[28] and the bMERB domain (PDB: 5LEO)[26].

Fig. 7: Phosphomimetic mutation of bMERB S960D does not affect Rab8 family member binding. a The schematic diagram of human Mical1 shows an N-terminal monooxygenase (MO) domain, a calponin homology (CH) domain, a Lin11, Isl-1, and Mec-3 (LIM) domain, and a C-terminal coiled-coil bMERB (bivalent Mical/EHBP Rab binding) domain, along with PAK1 phosphorylation sites S817 and S960. **b** The surface electrostatic potential of bMERB was calculated in PyMOL using the APBS-PDB2PQR plugin and visualized with colors ranging from red (-5 kT/e) to blue (+5 kT/e). AlphaFold2 predicted the Mical1 amino acids 807–820, with S817 shown in stick representation. The side chain of S817 points towards a negatively charged patch on the Mical1 bMERB domain. **c** Cartoon representation of the Mical1 bMERB domain (PDB: 5LPN)[28], with S960 shown in stick representation. Rab10 binding sites are indicated with dashed circles. **d, e, h-k** Binding of Rab8a (gray)/Rab10 (wheat)/Rab15 (red) with different Mical1 bMERB domain (green) was systematically tested onto a Superdex 75 10/300 GL column. **f, g, l-o** Binding affinities were measured by ITC experiments. Binding affinities were measured by titrating the Rab8/Rab10/Rab15 (600 µM) to wild type/mutant bMERB domain (30 µM). Integrated heat peaks were fitted to a two-site-binding model yielding the binding stoichiometry (N), the enthalpy (ΔH), the entropy (ΔS), and the dissociation constant (K_D). Phosphomimetic mutation of S960 of the bMERB domain does not affect interaction with Rab8/Rab10/Rab15. The data are representative of at least three repetitions.

Fig. 8: Impact of Rab binding site mutations in the bMERB domain on MO-CH-LIM interaction. a Schematic illustration of the interactions between the MO-CH-LIM domain and the bMERB domain. Hydrophobic interactions are indicated by light orange dashed lines, and hydrogen bonds are indicated by gray dashed lines. **b-i** Effect of RBS mutants on MO-CH-LIM:bMERB domain interaction. The binding of MO-CH-LIM with different RBS bMERB mutants was systematically tested, and affinities were determined by ITC experiments. Integrated heat peaks, corrected for the offset by subtracting the control experiment, were fitted to a one-site-binding model, yielding the binding stoichiometry (N), enthalpy (ΔH), entropy (ΔS), and dissociation constant (K_D). N.D. denotes not detected. The data are representative of at least three repetitions.

Fig. 9: Structural basis of Mical1 activation upon Rab8 binding. a Structural superposition of the Mical1 auto-inhibited AlphaFold2 model and the bMERB:Rab10 complex (PDB: 5LPN)[28]. **b** Structural overlay clearly shows that the binding of the first Rab molecule at high affinity stabilizes the helix 3 conformation, which structurally interferes with the CH domain and $Helix^{CHL}$ binding site. Additionally,

the movement of helices 1-2 strictly hinders the CH binding site. **c** The superimposition of the bMERB domain of Mical1 in the auto-inhibited AlphaFold2 model with the bMERB domain of the bMERB:Rab10 complex (PDB: 5LPN)[28] reveals the movement of bMERB helices upon Rab binding. **d** Structural overlay of the bMERB domain of Mical1 in the auto-inhibited state Alphafold2 model with the bMERB domain of the bMERB:Rab10 complex (PDB: 5LPN)[28], with an inset highlighting the conformational changes of interface residues upon Rab10 binding. **e** The results of systematic analysis of interactions between full-length Mical1 or different Mical1 deletion constructs with F-actin via co-sedimentation experiments reveal that the MO domain is the minimal domain required for interaction with F-actin, whereas the full-length Mical1 exhibits perturbed interaction with F-actin. These experiments were independently repeated at least three times with consistent results.

Fig. 10: The activation mechanism of Mical1 by Rab8 family members. In the absence of active Rab8, Mical1 exists in an auto-inhibited state, where the MO, CH, Helix^{CHL}, and LIM domains interact with its bMERB domain. Rab8 is recruited to the membrane by its GEF molecule (e.g., Rabin 8 or GRAB). The first molecule of active Rab8 binds to the high-affinity C-terminal binding site, leading to a change in the conformation of helix 3, which displaces the CH domain and Helix^{CHL}. The first binding of the Rab molecule also changes the conformation of helix 2 and helix 3 at the low-affinity N-terminal Rab binding site, further interfering with CH binding, and this conformation leads to a change in the LIM and MO binding interface on the bMERB domain, resulting in the displacement of the LIM and MO domains. The second Rab8 molecule binds to stabilize the active state of the enzyme, allowing the MO domain to be available for F-actin interaction, leading to the depolymerization of F-actin.

Fig1

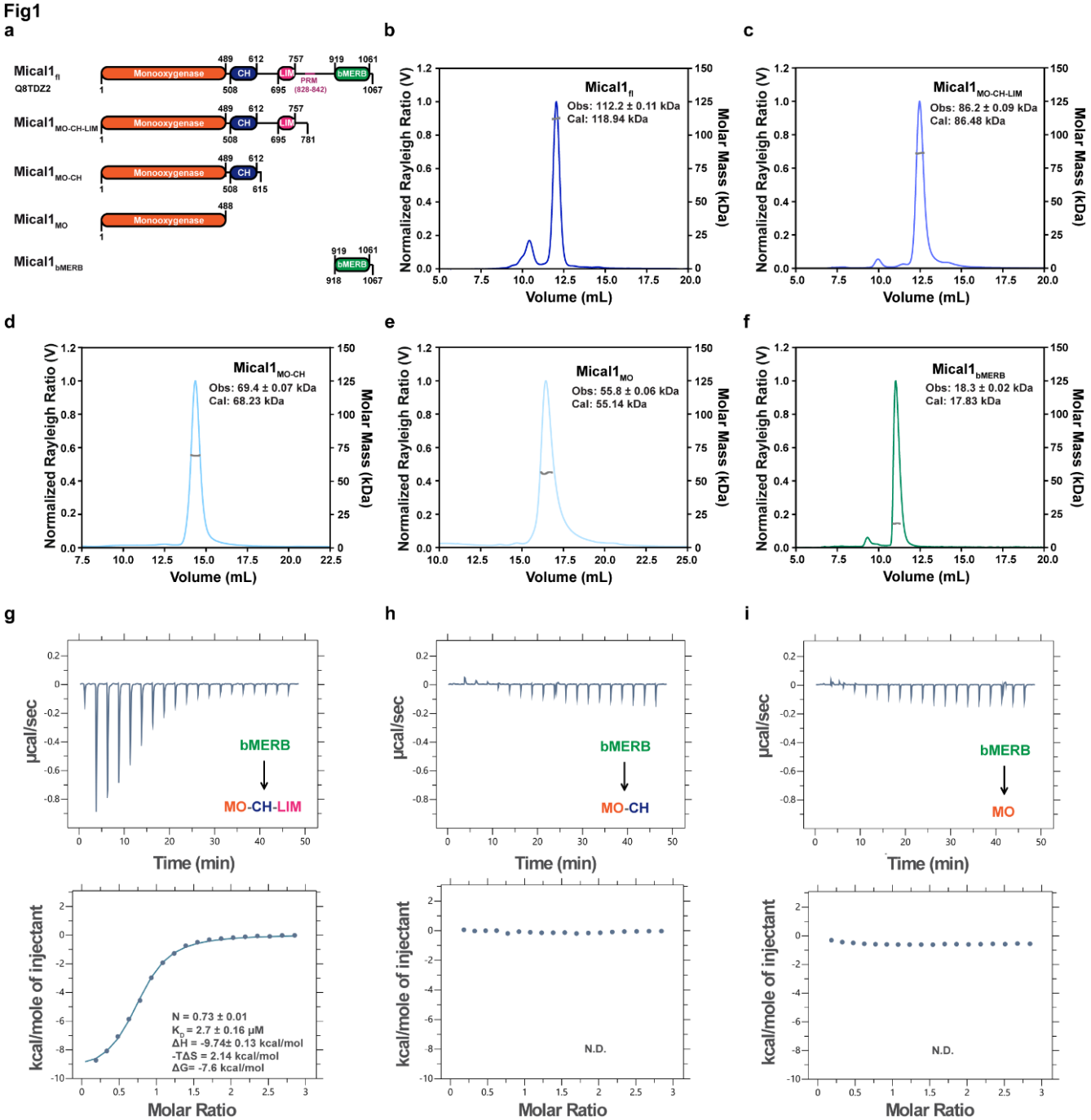
a
Mical1fl
Q8TDZ2
Monooxygenase
CH
LIM
PRM
(828-842)
bMERB
Mical1MO-CH-LIM
Mical1MO-CH
Mical1MO
Mical1bMERB
b
Mical1fl
Obs: 112.2 ± 0.11 kDa
Cal: 118.94 kDa
c
Mical1MO-CH-LIM
Obs: 86.2 ± 0.09 kDa
Cal: 86.48 kDa
d
Mical1MO-CH
Obs: 69.4 ± 0.07 kDa
Cal: 68.23 kDa
e
Mical1MO
Obs: 55.8 ± 0.06 kDa
Cal: 55.14 kDa
f
Mical1bMERB
Obs: 18.3 ± 0.02 kDa
Cal: 17.83 kDa
Normalized Rayleigh Ratio (V)
Molar Mass (kDa)
Volume (mL)
g
h
i
µcal/sec
Time (min)
bMERB
MO-CH-LIM
MO-CH
MO
kcal/mole of injectant
Molar Ratio
N = 0.73 ± 0.01
KD = 2.7 ± 0.16 µM
ΔH = -9.74± 0.13 kcal/mol
-TΔS = 2.14 kcal/mol
ΔG= -7.6 kcal/mol
N.D.

Fig2

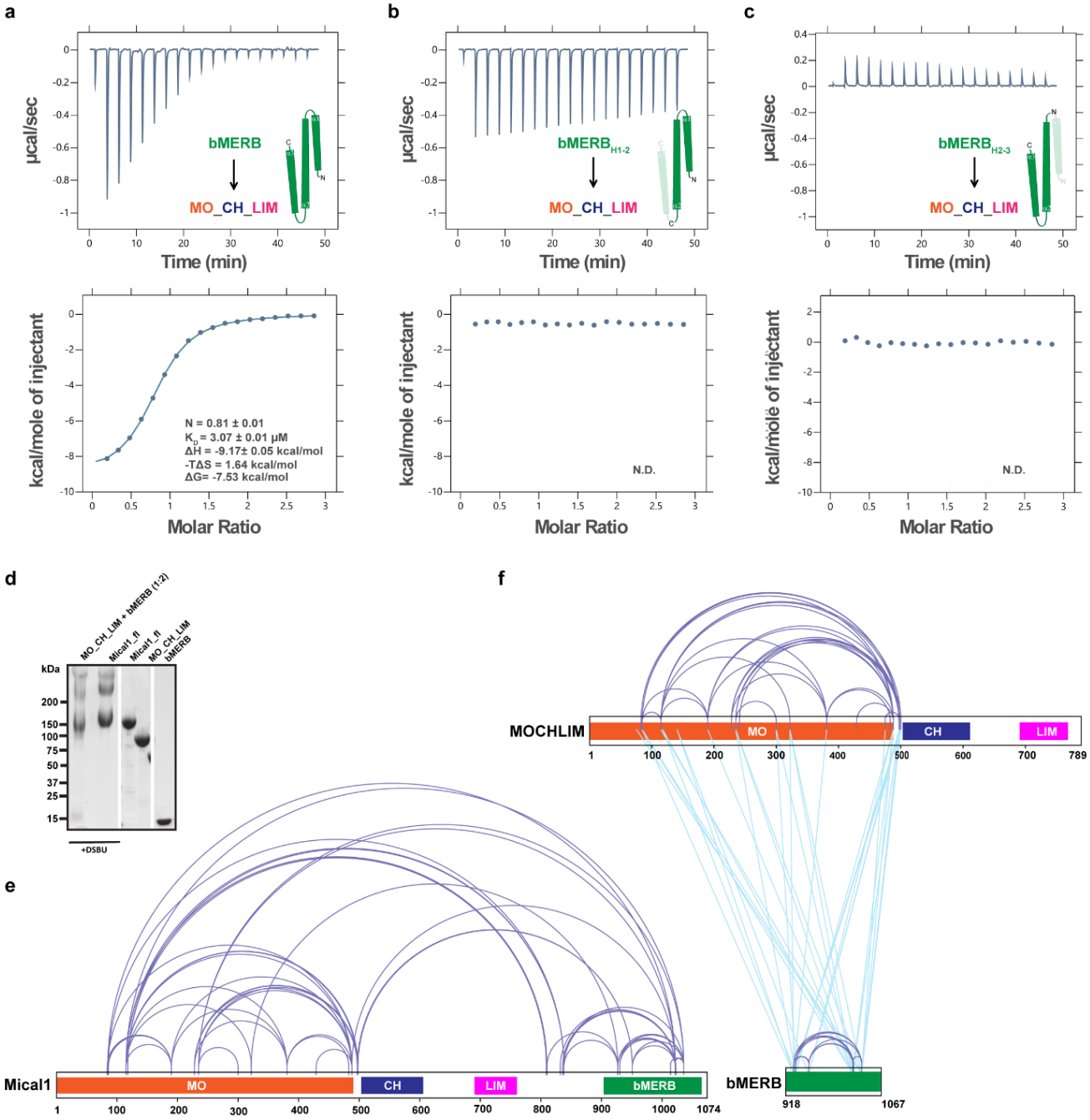
a
b
c
µcal/sec
Time (min)
bMERB
MO_CH_LIM
bMERB H1-2
bMERB H2-3
kcal/mole of injectant
Molar Ratio
N = 0.81 ± 0.01
K_D = 3.07 ± 0.01 µM
ΔH = -9.17± 0.05 kcal/mol
-TΔS = 1.64 kcal/mol
ΔG= -7.53 kcal/mol
N.D.
d
MO_CH_LIM + bMERB (1:2)
Mical1_fl
Mical1_fl
MO_CH_LIM
bMERB
kDa
+DSBU
e
Mical1
MO
CH
LIM
bMERB
f
MOCHLIM
bMERB

Fig3

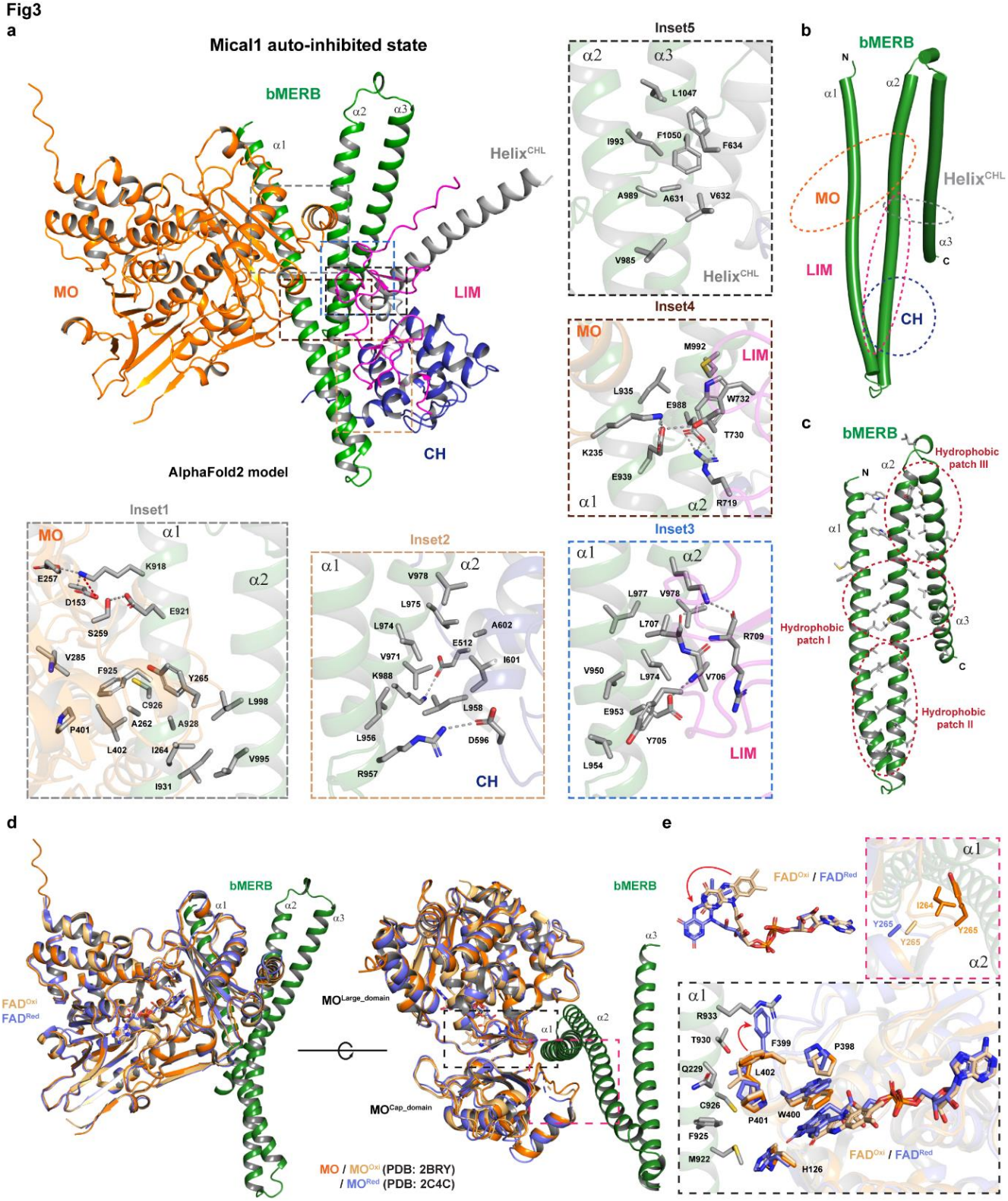

f

PISA	MO (1-488 aa)	CH (508-613 aa)	Helix^{CHL} (624-654 aa)	LIM (692-751 aa)	Linker (800-855 aa)	bMERB (886-1067 aa)
MO (1-488 aa)	—			310.9 Å²	381.2 Å²	1190 Å²
CH (508-613 aa)		—	297.8 Å²	309.6 Å²		506.5 Å²
Helix^{CHL} (624-654 aa)			—	255 Å²		462.6 Å²
LIM (692-751 aa)				—		652.4 Å²
Linker (800-855 aa)					—	158.1 Å²

Fig4

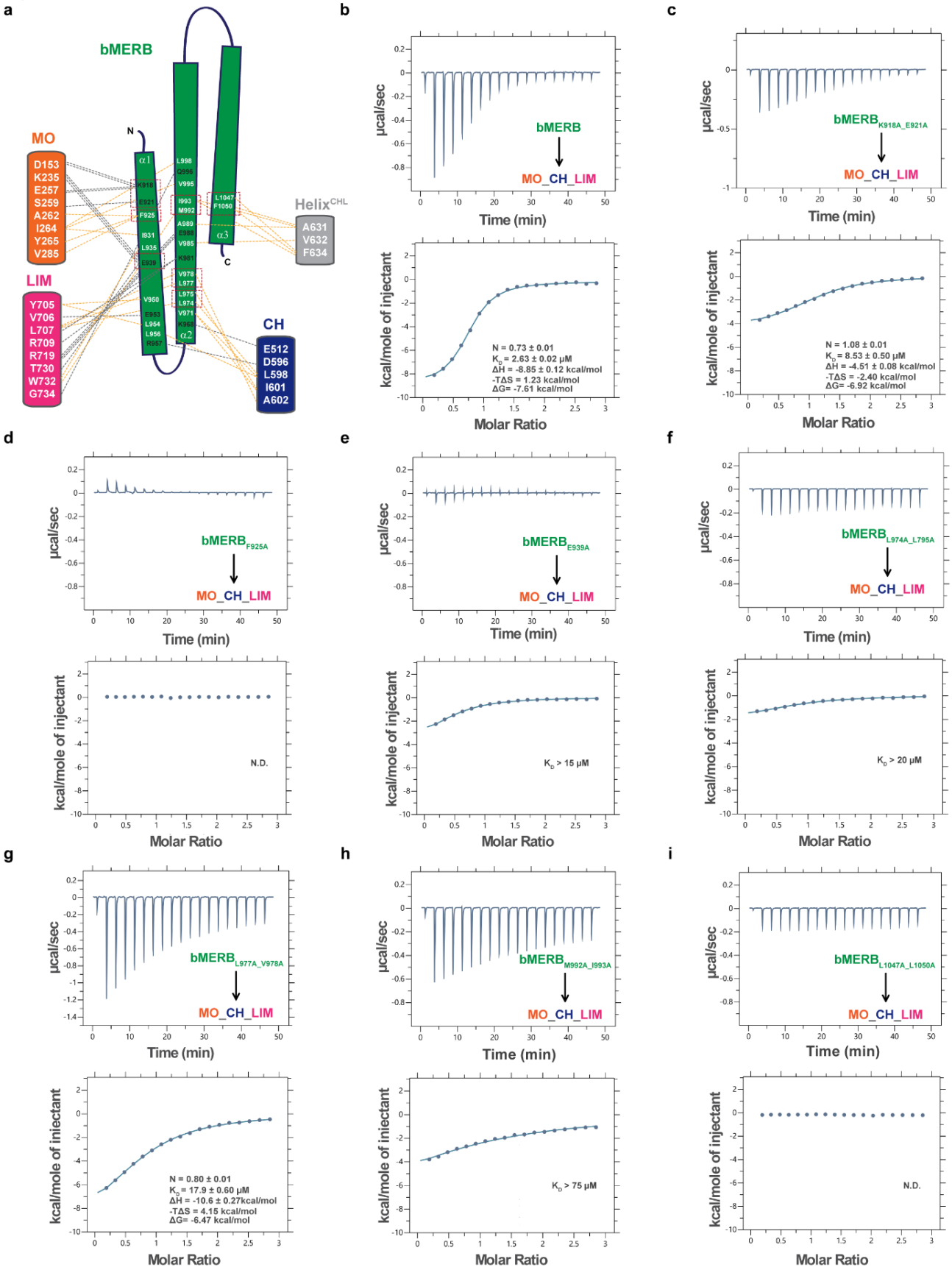
a
bMERB
MO
D153
K235
E257
S259
A262
I264
Y265
V285
LIM
Y705
V706
L707
R709
R719
T730
W732
G734
Helix^CHL
A631
V632
F634
CH
E512
D596
L598
I601
A602
b
bMERB
MO_CH_LIM
N = 0.73 ± 0.01
K_D = 2.63 ± 0.02 μM
ΔH = -8.85 ± 0.12 kcal/mol
-TΔS = 1.23 kcal/mol
ΔG= -7.61 kcal/mol
c
bMERB_K918A_E921A
MO_CH_LIM
N = 1.08 ± 0.01
K_D = 8.53 ± 0.50 μM
ΔH = -4.51 ± 0.08 kcal/mol
-TΔS = -2.40 kcal/mol
ΔG= -6.92 kcal/mol
d
bMERB_F925A
MO_CH_LIM
N.D.
e
bMERB_E939A
MO_CH_LIM
K_D > 15 μM
f
bMERB_L974A_L795A
MO_CH_LIM
K_D > 20 μM
g
bMERB_L977A_V978A
MO_CH_LIM
N = 0.80 ± 0.01
K_D = 17.9 ± 0.60 μM
ΔH = -10.6 ± 0.27kcal/mol
-TΔS = 4.15 kcal/mol
ΔG= -6.47 kcal/mol
h
bMERB_M992A_I993A
MO_CH_LIM
K_D > 75 μM
i
bMERB_L1047A_L1050A
MO_CH_LIM
N.D.
μcal/sec
Time (min)
kcal/mole of injectant
Molar Ratio

Fig5

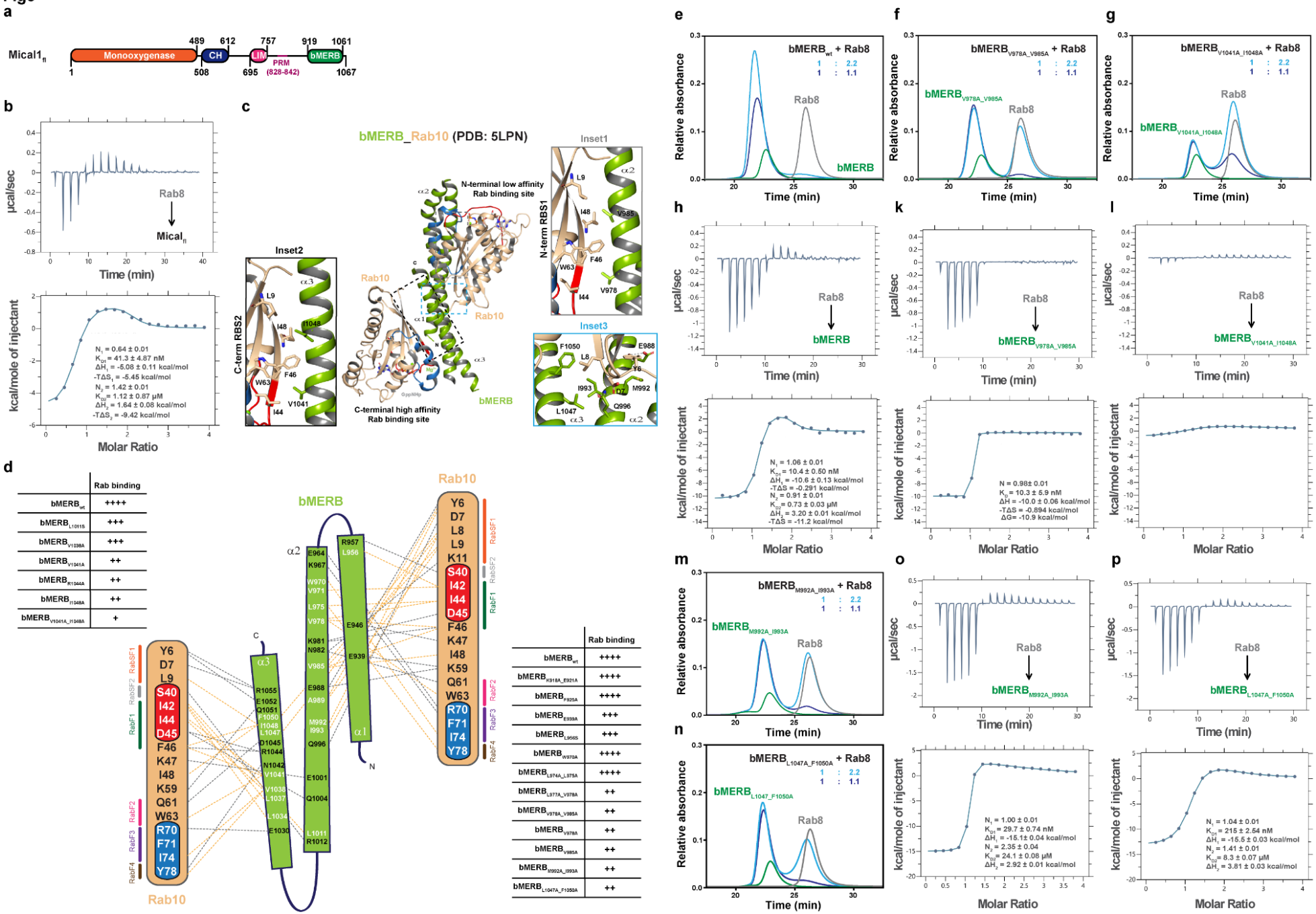
a
Mical1fl
Monooxygenase
CH
LIM
PRM (828-842)
bMERB
489 612 757 919 1061
1 508 695 1067
b
Rab8
Micalfl
Time (min)
kcal/mole of injectant
Molar Ratio
N1 = 0.64 ± 0.01
KD1 = 41.3 ± 4.87 nM
ΔH1 = -5.08 ± 0.11 kcal/mol
-TΔS1 = -5.45 kcal/mol
N2 = 1.42 ± 0.01
KD2 = 1.12 ± 0.87 μM
ΔH2 = 1.64 ± 0.08 kcal/mol
-TΔS2 = -9.42 kcal/mol
c
bMERB_Rab10 (PDB: 5LPN)
N-terminal low affinity Rab binding site
C-terminal high affinity Rab binding site
Rab10
bMERB
Inset1
Inset2
Inset3
N-term RBS1
C-term RBS2
d
Rab binding
bMERBwt ++++
bMERBL1011S +++
bMERBV1039A +++
bMERBV1041A ++
bMERBR1044A ++
bMERBI1048A ++
bMERBV1041A_I1048A +
Rab binding
bMERBwt ++++
bMERBK918A_E921A ++++
bMERBF925A ++++
bMERBE939A +++
bMERBL956S +++
bMERBW970A ++++
bMERBL974A_L975A ++++
bMERBL977A_V978A ++
bMERBV978A_V985A ++
bMERBV978A ++
bMERBV985A ++
bMERBM992A_I993A ++
bMERBL1047A_F1050A ++
e
bMERBwt + Rab8
1 : 2.2
1 : 1.1
Rab8
bMERB
Relative absorbance
Time (min)
f
bMERBV978A_V985A + Rab8
bMERBV978A_V985A
g
bMERBV1041A_I1048A + Rab8
bMERBV1041A_I1048A
h
k
l
N1 = 1.06 ± 0.01
KD1 = 10.4 ± 0.50 nM
ΔH1 = -10.6 ± 0.13 kcal/mol
-TΔS = -0.291 kcal/mol
N2 = 0.91 ± 0.01
KD2 = 0.73 ± 0.03 μM
ΔH2 = 3.20 ± 0.01 kcal/mol
-TΔS = -11.2 kcal/mol
N = 0.98± 0.01
KD = 10.3 ± 5.9 nM
ΔH = -10.0 ± 0.06 kcal/mol
-TΔS = -0.894 kcal/mol
ΔG= -10.9 kcal/mol
m
bMERBM992A_I993A + Rab8
bMERBM992A_I993A
o
p
bMERBL1047A_F1050A
n
bMERBL1047A_F1050A + Rab8
bMERBL1047_F1050A
N1 = 1.00 ± 0.01
KD1 = 29.7 ± 0.74 nM
ΔH1 = -15.1± 0.04 kcal/mol
N2 = 2.35 ± 0.04
KD2 = 24.1 ± 0.08 μM
ΔH2 = 2.92 ± 0.01 kcal/mol
N1 = 1.04 ± 0.01
KD1 = 215 ± 2.54 nM
ΔH1 = -15.5 ± 0.03 kcal/mol
N2 = 1.41 ± 0.01
KD2 = 8.3 ± 0.07 μM
ΔH2 = 3.81 ± 0.03 kcal/mol

Fig6

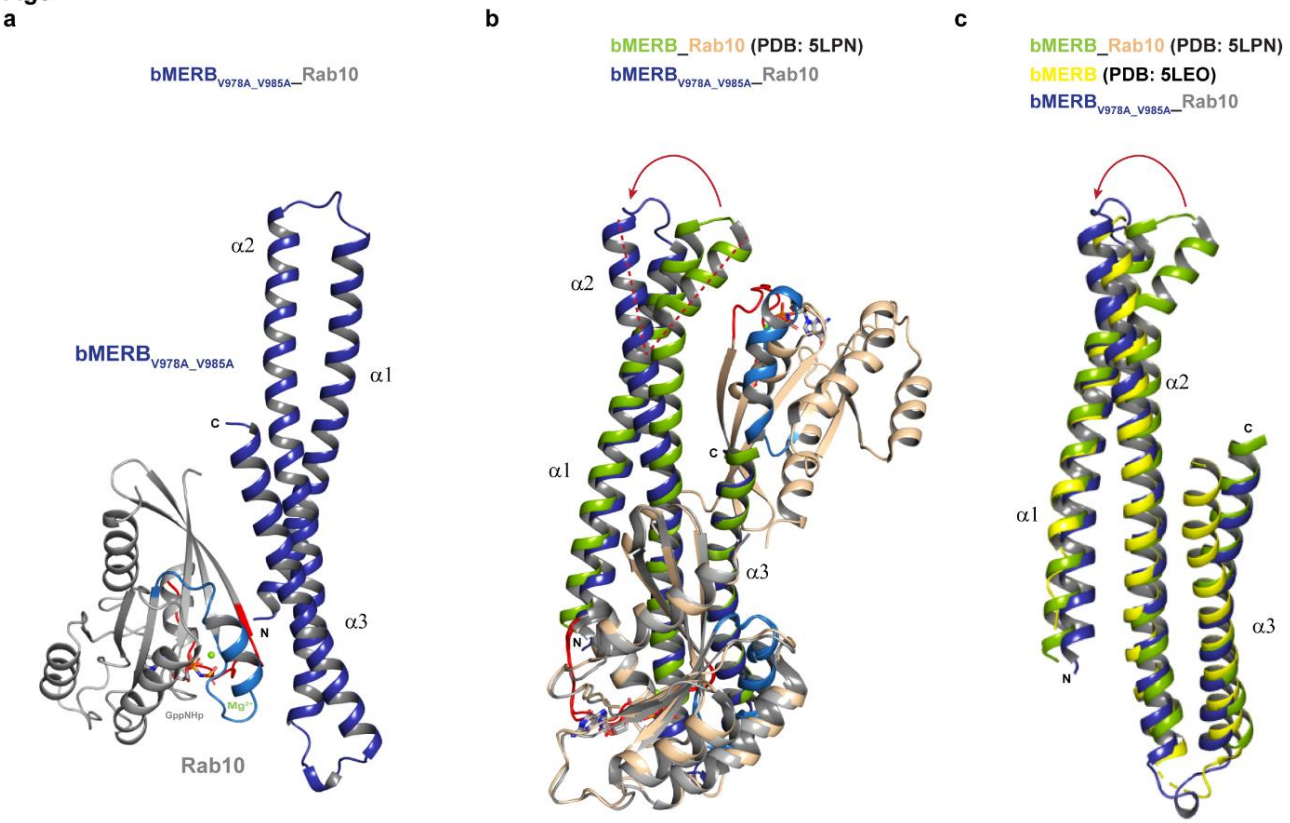
a
bMERB$_{V978A_V985A}$–Rab10
α2
bMERB$_{V978A_V985A}$
α1
C
N
α3
GppNHp
Mg^{2+}
Rab10
b
bMERB_Rab10 (PDB: 5LPN)
bMERB$_{V978A_V985A}$–Rab10
α2
α1
C
α3
N
c
bMERB_Rab10 (PDB: 5LPN)
bMERB (PDB: 5LEO)
bMERB$_{V978A_V985A}$–Rab10
α2
C
α1
α3
N

Fig7

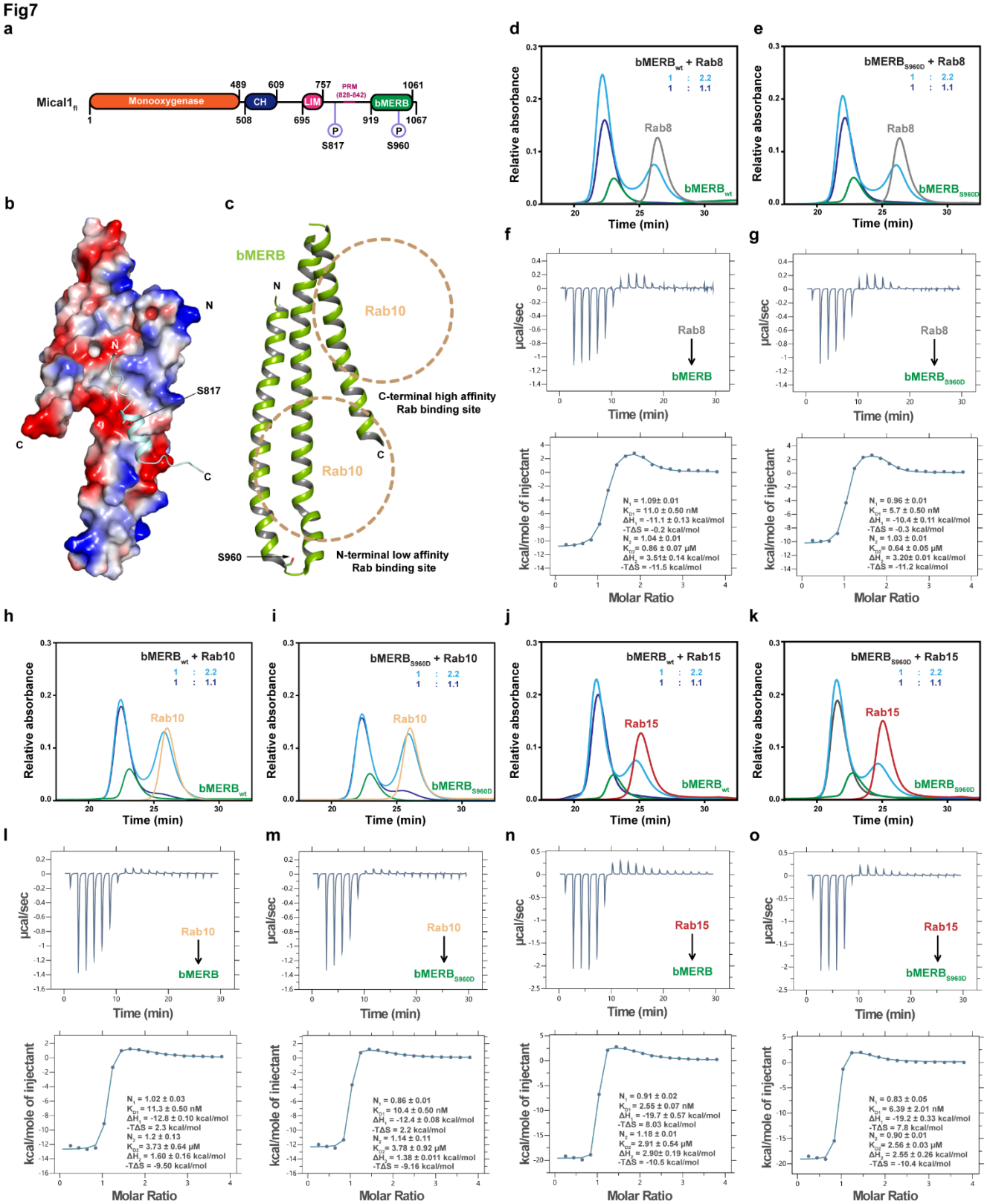
a
Mical1fl
Monooxygenase
CH
LIM
PRM (828-842)
bMERB
489
609
757
1061
1
508
695
919
1067
P
S817
S960
b
N
S817
C
c
bMERB
Rab10
C-terminal high affinity Rab binding site
N-terminal low affinity Rab binding site
S960
d
bMERBwt + Rab8
1 : 2.2
1 : 1.1
Rab8
bMERBwt
Relative absorbance
Time (min)
e
bMERBS960D + Rab8
bMERBS960D
f
µcal/sec
Rab8
bMERB
kcal/mole of injectant
Molar Ratio
N1 = 1.09± 0.01
K21 = 11.0 ± 0.50 nM
ΔH1 = -11.1 ± 0.13 kcal/mol
-TΔS = -0.2 kcal/mol
N2 = 1.04 ± 0.01
K22 = 0.86 ± 0.07 µM
ΔH2 = 3.51± 0.14 kcal/mol
-TΔS = -11.5 kcal/mol
g
bMERBS960D
N1 = 0.96 ± 0.01
K21 = 5.7 ± 0.50 nM
ΔH1 = -10.4 ± 0.11 kcal/mol
-TΔS = -0.3 kcal/mol
N2 = 1.03 ± 0.01
K22 = 0.64 ± 0.05 µM
ΔH2 = 3.20± 0.01 kcal/mol
-TΔS = -11.2 kcal/mol
h
bMERBwt + Rab10
i
bMERBS960D + Rab10
j
bMERBwt + Rab15
Rab15
k
bMERBS960D + Rab15
l
N1 = 1.02 ± 0.03
K21 = 11.3 ± 0.50 nM
ΔH1 = -12.8 ± 0.10 kcal/mol
-TΔS = 2.3 kcal/mol
N2 = 1.2 ± 0.13
K22 = 3.73 ± 0.64 µM
ΔH2 = 1.60 ± 0.16 kcal/mol
-TΔS = -9.50 kcal/mol
m
N1 = 0.86 ± 0.01
K21 = 10.4 ± 0.50 nM
ΔH1 = -12.4 ± 0.08 kcal/mol
-TΔS = 2.2 kcal/mol
N2 = 1.14 ± 0.11
K22 = 3.78 ± 0.92 µM
ΔH2 = 1.38 ± 0.011 kcal/mol
-TΔS = -9.16 kcal/mol
n
N1 = 0.91 ± 0.02
K21 = 2.55 ± 0.07 nM
ΔH1 = -19.7 ± 0.57 kcal/mol
-TΔS = 8.03 kcal/mol
N2 = 1.18 ± 0.01
K22 = 2.91 ± 0.54 µM
ΔH2 = 2.90± 0.19 kcal/mol
-TΔS = -10.5 kcal/mol
o
N1 = 0.83 ± 0.05
K21 = 6.39 ± 2.01 nM
ΔH1 = -19.2 ± 0.33 kcal/mol
-TΔS = 7.8 kcal/mol
N2 = 0.90 ± 0.01
K22 = 2.56 ± 0.03 µM
ΔH2 = 2.55 ± 0.26 kcal/mol
-TΔS = -10.4 kcal/mol

Fig8

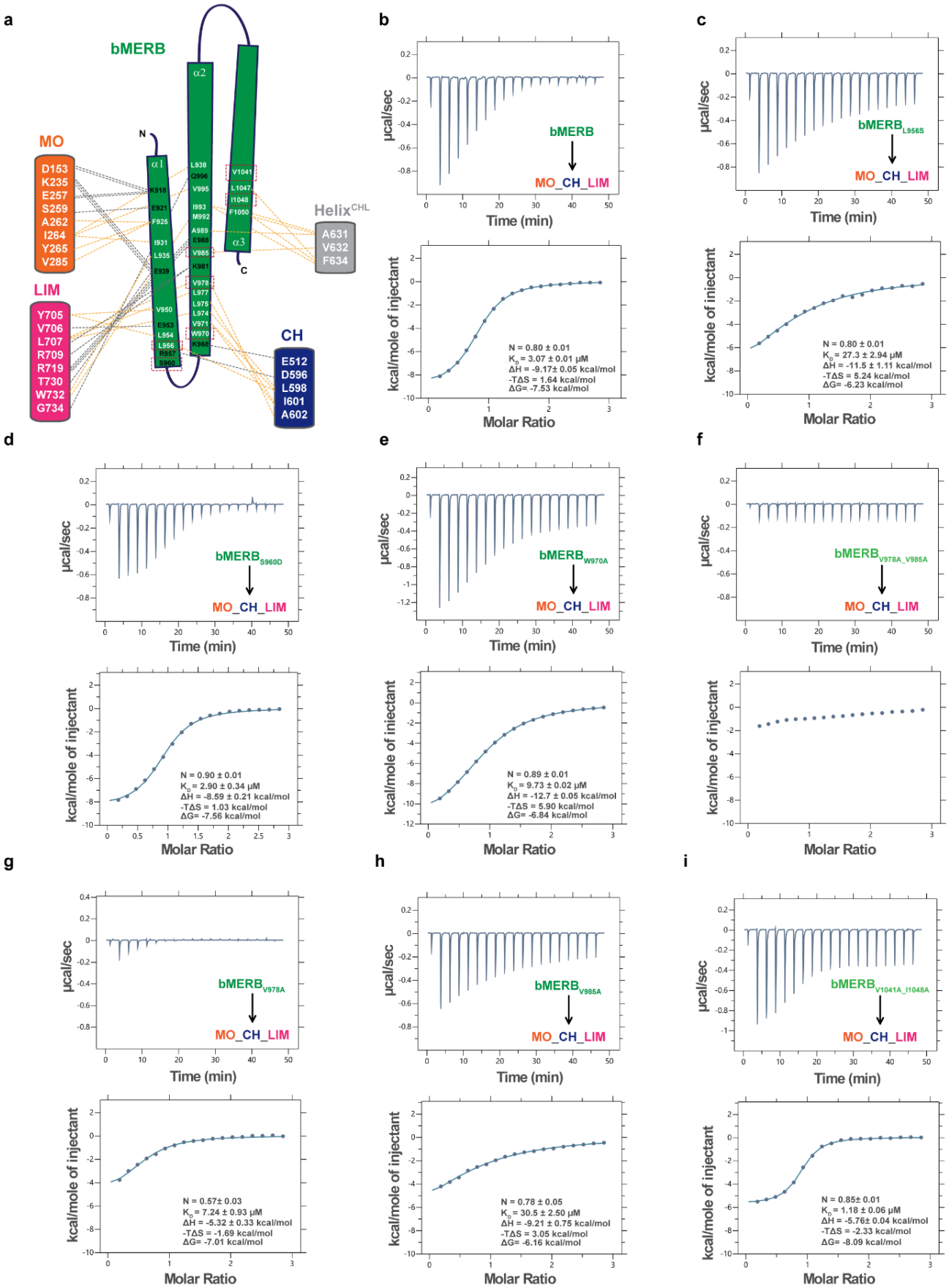
a
bMERB
α2
α1
α3
N
C
MO
D153
K235
E257
S259
A262
I264
Y265
V285
LIM
Y705
V706
L707
R709
R719
T730
W732
G734
HelixCHL
A631
V632
F634
CH
E512
D596
L598
I601
A602
b
bMERB
MO_CH_LIM
Time (min)
µcal/sec
kcal/mole of injectant
Molar Ratio
N = 0.80 ± 0.01
KD = 3.07 ± 0.01 µM
ΔH = -9.17± 0.05 kcal/mol
-TΔS = 1.64 kcal/mol
ΔG= -7.53 kcal/mol
c
bMERBL956S
MO_CH_LIM
N = 0.80 ± 0.01
KD = 27.3 ± 2.94 µM
ΔH = -11.5 ± 1.11 kcal/mol
-TΔS = 5.24 kcal/mol
ΔG= -6.23 kcal/mol
d
bMERBS960D
MO_CH_LIM
N = 0.90 ± 0.01
KD = 2.90 ± 0.34 µM
ΔH = -8.59 ± 0.21 kcal/mol
-TΔS = 1.03 kcal/mol
ΔG= -7.56 kcal/mol
e
bMERBW970A
MO_CH_LIM
N = 0.89 ± 0.01
KD = 9.73 ± 0.02 µM
ΔH = -12.7 ± 0.05 kcal/mol
-TΔS = 5.90 kcal/mol
ΔG= -6.84 kcal/mol
f
bMERBV978A_V985A
MO_CH_LIM
g
bMERBV978A
MO_CH_LIM
N = 0.57± 0.03
KD = 7.24 ± 0.93 µM
ΔH = -5.32 ± 0.33 kcal/mol
-TΔS = -1.69 kcal/mol
ΔG= -7.01 kcal/mol
h
bMERBV985A
MO_CH_LIM
N = 0.78 ± 0.05
KD = 30.5 ± 2.50 µM
ΔH = -9.21 ± 0.75 kcal/mol
-TΔS = 3.05 kcal/mol
ΔG= -6.16 kcal/mol
i
bMERBV1041A_I1048A
MO_CH_LIM
N = 0.85± 0.01
KD = 1.18 ± 0.06 µM
ΔH = -5.76± 0.04 kcal/mol
-TΔS = -2.33 kcal/mol
ΔG= -8.09 kcal/mol

Fig9

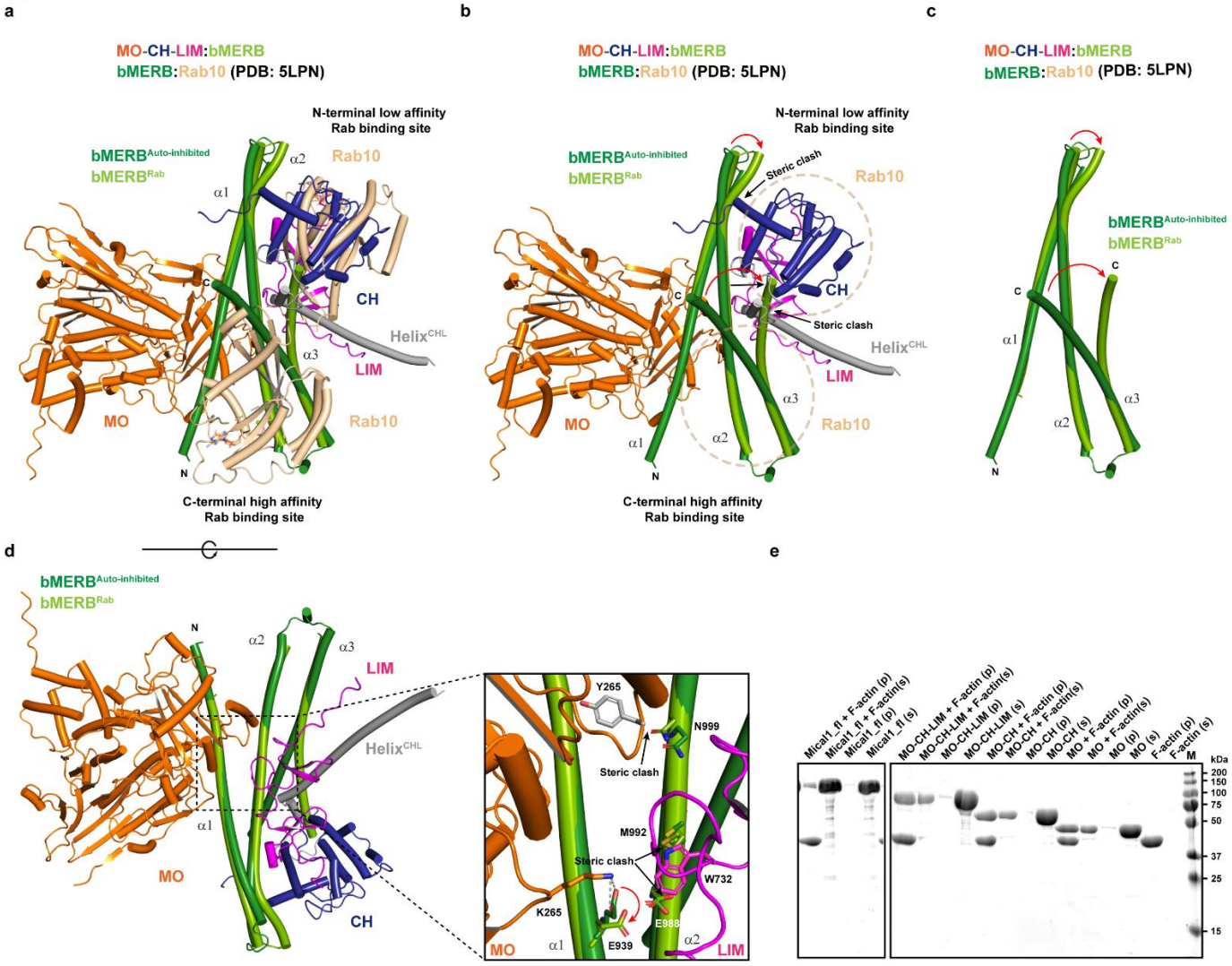
a
MO-CH-LIM:bMERB
bMERB:Rab10 (PDB: 5LPN)
N-terminal low affinity
Rab binding site
bMERBAuto-inhibited
bMERBRab
α2
Rab10
α1
CH
HelixCHL
α3
LIM
MO
Rab10
C-terminal high affinity
Rab binding site
b
MO-CH-LIM:bMERB
bMERB:Rab10 (PDB: 5LPN)
N-terminal low affinity
Rab binding site
bMERBAuto-inhibited
bMERBRab
Steric clash
Rab10
CH
Steric clash
HelixCHL
LIM
α3
MO
α1
α2
Rab10
C-terminal high affinity
Rab binding site
c
MO-CH-LIM:bMERB
bMERB:Rab10 (PDB: 5LPN)
bMERBAuto-inhibited
bMERBRab
α1
α3
α2
d
bMERBAuto-inhibited
bMERBRab
α2
α3
LIM
HelixCHL
α1
MO
CH
Y265
N999
Steric clash
M992
Steric clash
W732
K265
E988
E939
MO
α1
α2
LIM
e
Mical1_fl + F-actin (p)
Mical1_fl + F-actin(s)
Mical1_fl (p)
Mical1_fl (s)
MO-CH-LIM + F-actin (p)
MO-CH-LIM + F-actin(s)
MO-CH-LIM (p)
MO-CH-LIM (s)
MO-CH + F-actin (p)
MO-CH + F-actin(s)
MO-CH (p)
MO-CH (s)
MO + F-actin (p)
MO + F-actin(s)
MO (p)
MO (s)
F-actin (p)
F-actin (s)
M
kDa
200
150
100
75
50
37
25
15

Fig10

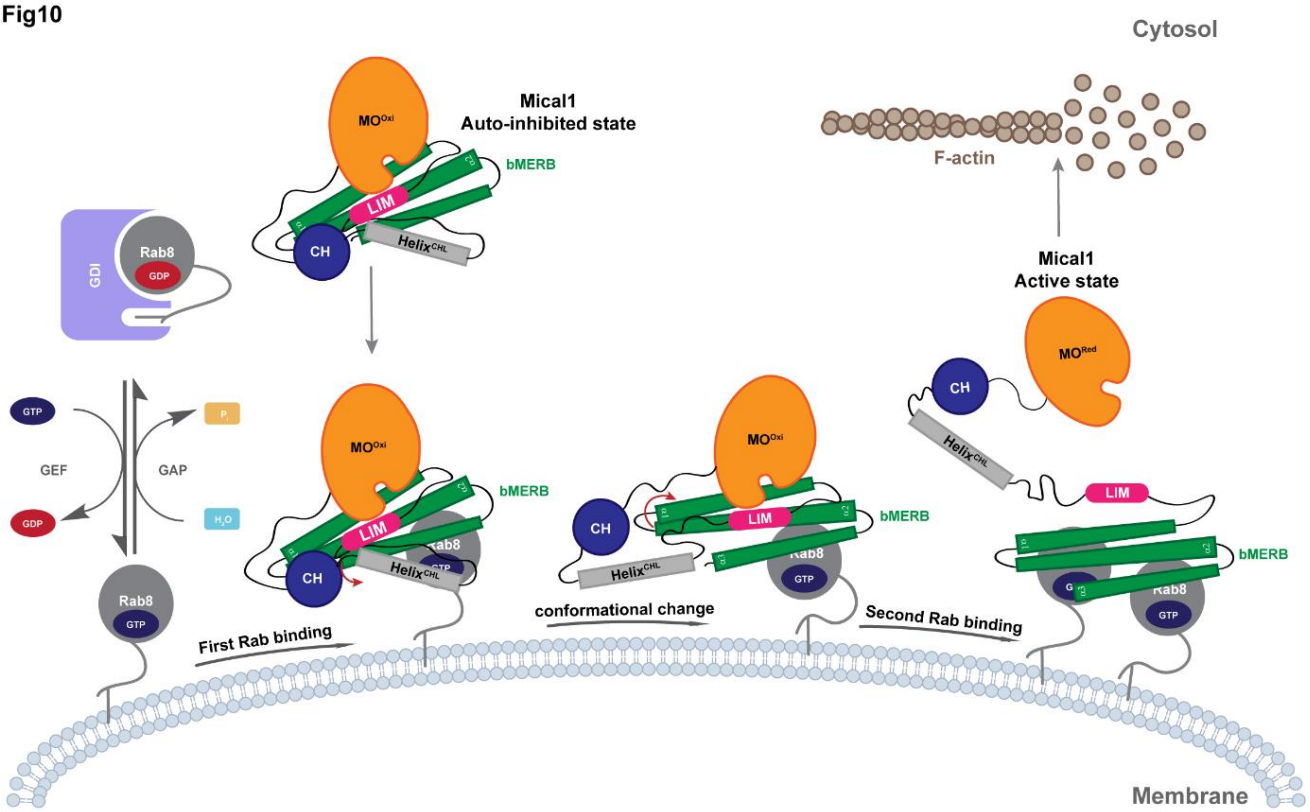
Cytosol
Mical1
Auto-inhibited state
MO^Oxi
bMERB
LIM
CH
Helix^CHL
F-actin
Mical1
Active state
MO^Red
GDI
Rab8
GDP
GTP
GEF
GAP
P_i
H_2O
First Rab binding
conformational change
Second Rab binding
Membrane